Materials Advances

ROYAL SOCIETY OF CHEMISTRY

PAPER

View Article Online
View Journal | View Issue

Cite this: *Mater. Adv.*, 2024, 5, 8709

Coal fly ash-ZIF composites for enhanced and stable carbon capture—an in-depth study†

Ramadurgam Aniruddha,[a] Satyapaul A Singh,[a] Benjaram M Reddy,[b] Akula Venugopal[c] and Inkollu Sreedhar*[a]

Composites possess significant potential to mitigate the shortcomings of their individual components, offering a measure of reinforcement. In this study, composites based on CFA based Na-A and ZIF-8 were synthesized and subjected to CO_2 adsorption tests. The composites were identified as a class of ZIF-8@Na-A. These composites retained the physical attributes of their parent materials. Notably, the CO_2 uptake performance of ZIF-8@Na-A (1 : 5) was particularly high, recording values around 3.48 mmol g^{-1} at 298 K and 1 bar. Hierarchical three step process optimization has been done to achieve the highest carbon capture and stability. Different synthesis protocols have been compared too. TGA studies have been used to validate the amine loading on the adsorbent. Among the factors influencing CO_2 uptake, temperature and pressure emerged as the most influential, while the time of carbonation exhibited minimal impact. Kinetic analysis revealed that the optimized adsorbent adhered to Avrami kinetics, displaying high R^2 values of 0.994. The Sips adsorption model demonstrated the best fit for explaining the adsorption behavior of the adsorbents. The average heat of adsorption for ZIF-8@Na-A was measured at −11 kJ mol^{-1}. During a 50-cycle stability assessment, the adsorbent exhibited robust performance, retaining approximately 92% of its initial CO_2 uptake. However, a subtle change in appearance was observed in the ZIF-8@Na-A adsorbent, which turned slightly pale yellowish after the completion of 50 cycles.

Received 8th June 2024,
Accepted 5th October 2024

DOI: 10.1039/d4ma00597j

rsc.li/materials-advances

1. Introduction

Metal organic frameworks (MOFs) have emerged as a pivotal class of materials in the field of carbon capture over the past two decades. This surge in their significance could be attributed to their remarkable characteristics, including but not limited to their expansive surface area (500–2000 m^2 g^{-1}), versatile functionality, modifiable pore structure, exceptional pore volumes (0.3 cc g^{-1} to 1.5 cc g^{-1}), presence of accessible metal sites, and the ability to tailor their morphology.[1] In order to address certain limitations associated with metal–organic frameworks (MOFs), including thermal instability, structural degradation in the presence of moisture, and limited cyclic regeneration capability, zeolitic imidazolate frameworks (ZIFs), a specific subclass of MOFs, have emerged as a viable alternative. ZIFs[2] have garnered significant attention in the scientific community due to their remarkable thermal stability, notable hydrophobicity, and exceptional physico-chemical characteristics.

Composites have recently garnered significant attention within the realm of adsorption and catalysis. Composite materials are meticulously fabricated with the objective of synergistically amalgamating the inherent strengths of distinct classes, thereby effectively concealing any inherent weaknesses that may be present. The synthesis of a composite material consisting of metal–organic framework (MOF) and graphene oxide was done by Wang and group[3] in their investigation on the adsorption of carbon dioxide (CO_2). The composite material was designated as the Mg/DOBDC MOF@GO composite, with different ratios being investigated. The group of composites exhibited remarkable carbon capture (CC) efficiency by synergistically leveraging the substantial surface area of the metal–organic framework (MOF) and the strong affinity of graphene oxide towards CO_2. The investigation conducted by Chang *et al.*[4] focused on the examination of composites possessing a dual nature, consisting of magnesium oxide (MgO) and zinc oxide (ZnO), incorporated within zeolitic imidazolate framework-8 (ZIF-8). The composites exhibited remarkable carbon capture (CC) uptake values (1.3 mmol g^{-1}) in comparison to ZIF-8 in its pure form (0.81 mmol g^{-1}), while simultaneously preserving the favorable morphological characteristics of ZIF-8. In the study conducted by

[a] *Department of Chemical Engineering, BITS Pilani Hyderabad Campus, Hyderabad, India. E-mail: isreedhar@hyderabad.bits-pilani.ac.in; Fax: +91 4066303998; Tel: +91 4066303512*
[b] *Department of Chemistry, BITS Pilani Hyderabad Campus, Hyderabad, India*
[c] *I&PC Division, IICT Tarnaka, Hyderabad, India*

† Electronic supplementary information (ESI) available. See DOI: https://doi.org/10.1039/d4ma00597j

Tari and team,[5] an innovative composite material named Cu-BDC/MCM-41 was synthesized, combining a stable metal–organic framework (MOF) with MCM-41. The composite material presented in this study exhibits a unique amalgamation of mesoporous and microporous structures, resulting in a significant enhancement of CO_2 adsorption capabilities (7.00 mmol g^{-1}) compared to its constituent materials. In our recent investigation,[6] the focus was directed towards the exploration of coal fly ash as a potential resource for the production of value-added materials. Specifically, a composite material (CC uptake of 2.83 mmol g^{-1}) comprising coal fly ash zeolite and ZIF-8 was synthesized and subsequently employed for the purpose of investigating its efficacy in CO_2 adsorption. The corresponding investigation yielded noteworthy findings regarding the synergistic effect of combining zeolite and ZIF-8 on the uptake of carbon dioxide (CC). The current investigation represents a seamless extension of prior research endeavors, with a primary focus on elucidating the process of synthesizing and employing innovative composite materials.

Coal fly ash (CFA) is a widely encountered and potentially consequential byproduct arising from diverse industrial operations. The potential of this substance as a precursor in the advancement of commercial adsorbents tailored for the purification of gaseous pollutants has been extensively investigated by researchers.[7] The appeal of CFA resides in its broad accessibility and cost-efficiency, both of which serve as crucial factors in facilitating comprehensive explorations of its extensive applicability in sorbent synthesis.[8] A range of compositions are available for use as adsorbents made from coal fly ash.[9] The diverse assortment of artificially produced adsorbents serves as a compelling testament to the multifaceted characteristics exhibited by coal fly ash.

The current investigation expands upon previous scholarly endeavors by exploring the synthesis and utilization of innovative composite materials. The present study encompasses the fabrication of composite structures, wherein ZIF-8 and Na-A are combined and subsequently subjected to tetraethylenepentaamine (TEPA) modification. Engineering dual-textured composites was the reasoning for the combination of Na-A and ZIF-8. Zeolitic imidazolate frameworks, in general, have been found to possess predominantly microporous properties, which make them highly effective in rapidly adsorbing CO_2, as demonstrated by Pokhrel.[10] Their high surface area and microporosity also make them potentially suitable candidates for amine modification. Materials with high specific surface area, such as ZIFs and MOFs, hold significant potential as hosts for amines due to their extensive porosity and structural diversity. However, the inherent microporous nature of these materials presents distinct challenges when it comes to amine loading. The narrow and confined pore structures typical of these materials can make it difficult to achieve uniform amine distribution throughout the porous network. This issue is exacerbated by the fact that, in many cases, the amine molecules must navigate through intricate pathways within the micropores, which can lead to incomplete or uneven loading. Moreover, the process of impregnating these materials with amines often requires prolonged interaction times. The slow diffusion of amines into the microporous structure means that achieving an optimal loading level is typically a time-intensive process. This extended duration is crucial, as insufficient interaction time can result in under-utilization of the available surface area, thereby diminishing the material's potential for CO_2 capture. Despite these challenges, successful amine loading onto the extensive surface area of microporous materials can significantly enhance their performance in selective CO_2 sorption. When adequately impregnated, the large surface area provided by materials like ZIFs and MOFs allows for a greater quantity of amine molecules to be anchored within the pores. This, in turn, increases the availability of active sites for CO_2 adsorption, thereby improving the selectivity and capacity of the material for CO_2 capture from mixed gas streams.

Primary amines, such as monoethanolamine and diethanolamine, have traditionally been utilized for the purpose of carbon dioxide absorption from feed streams owing to their convenient synthesis and comparatively lower activation energies. The present state of scientific investigation reveals that amines, such as diethanolamine (DEA) and TEPA, persist as preferred choices to be loaded onto neutral supports. Polymer-based fundamental compounds, exemplified by polyethylenimine (PEI)[11–13] and 3-aminopropyltrimethoxysilane (APTMS), have recently surfaced in the realm of synthesizing composite materials. The exceptional affinity of these organic basic compounds towards acidic gaseous pollutants endows them with remarkable versatility and potential in the absorption processes of gaseous pollutants such as carbon dioxide (CO_2) and sulfur dioxide (SO_2).[14] Moreover, the inherent characteristic of these substances renders them highly suitable for their impregnation onto high surface area sorbents such as activated carbons and porous organic frameworks, thereby significantly broadening their scope of potential applications. Significantly, aminopropyltrimethoxysilane (APTMS) was employed by Sara Ahsan and colleagues[15] in their investigation on carbon dioxide (CO_2) capture, specifically focusing on the application of zeolite-5 adsorbents. The experimental findings revealed an impressive carbon capture capacity of approximately 5.7 weight percent (wt%).

The outlet pressures of flue gases, typically maintained just above atmospheric levels (1 to 10 kPa above ambient pressure),[16–18] are crucial for system efficiency, environmental compliance, and safe operation in industrial settings. Industrial flue gas, a byproduct of combustion processes in industries like power plants and cement production, typically contains a mix of gases and particles. Its main components include nitrogen (65–75%), carbon dioxide (10–20%), water vapor (5–15%), and oxygen (3–8%), along with smaller amounts of sulfur dioxide (SO_2), nitrogen oxides (NOx), carbon monoxide (CO), particulate matter, and trace elements like heavy metals and volatile organic compounds (VOCs).[19–21] The composition varies based on the fuel and process, impacting the design of pollution control systems and carbon capture technologies.

Typically, CO_2 removal from flue gases *via* adsorption is conducted at or near atmospheric pressure (around 1 bar), as this corresponds to the typical exit pressure of flue gas streams in most industrial plants, with recovery of adsorbents done

through temperature swing process.[22] Operating at this pressure minimizes the need for additional energy input, making it a practical choice for many carbon capture processes. However, emerging capture technologies are increasingly exploring the use of higher process pressures, ranging from 4 bar to 10 bar.[23] While maintaining an adsorber at such elevated pressures does require significantly more energy, this approach offers certain advantages. Notably, the recovery of CO_2 from these high-pressure conditions is relatively straightforward, as the higher pressure can enhance the adsorption capacity and improve the efficiency of the capture process. An even more advanced and extreme approach involves the use of vacuum-assisted recovery following high-pressure CO_2 adsorption.[24–26] In this scenario, after CO_2 is captured at pressures as high as 10 bar, a vacuum is applied to the system to facilitate the desorption of CO_2 from the adsorbent material. This vacuum process helps to efficiently recover the CO_2 by reducing the pressure, thereby driving the release of the gas from the adsorbent. Although this method requires sophisticated equipment and careful energy management, it can be highly effective in maximizing CO_2 recovery, particularly in processes where high-pressure capture is used to enhance adsorption performance.

Proper pressure control ensures the effective performance of flue gas treatment systems, such as carbon capture units, while also optimizing the operation of downstream equipment like gas turbines and CHP systems. Maintaining appropriate outlet pressures helps to ensure that emission control devices function effectively, reducing pollutants like SOx, NOx, particulate matter, and CO_2. Additionally, managing outlet pressures is a safety concern, as excessive pressure can lead to dangerous conditions, necessitating the use of pressure relief valves and other safety mechanisms. Optimized outlet pressures also contribute to energy efficiency by minimizing the operational costs of fans and blowers. Herein, the pressures of typical flue gases along with elevated pressures were considered to evaluate the heat of adsorption of the system.

The present study is focused on the examination of adsorption phenomena within the confines of a fixed bed reactor system. In order to optimize the precision and effectiveness of the conducted experiments, the present study utilized the response surface methodology (RSM) in tandem with a face-centered central composite design (CCD) as the chosen experimental design strategy. It is important to note that the carbon capture performance of an adsorbent is subject to the influence of various factors, including but not limited to the amine loading percentage, adsorbent weight, and temperature. It is noteworthy to acknowledge that traditional experimental designs frequently isolate these factors in order to investigate them individually, inadvertently neglecting the intricate interconnections that exist among them. Response surface methodology (RSM), however, surpasses these limitations by encompassing the simultaneous consideration of the combined effects of all aforementioned variables. Through the utilization of regression analysis, response surface methodology (RSM) facilitates the comprehensive evaluation of the combined impact of these factors on the adsorption process. This ultimately culminates in the identification of the most favourable process conditions. The implementation of this all-encompassing methodology not only amplifies accuracy but also diminishes the necessity for a substantial quantity of trials, thus preserving precious assets such as time, financial capital, chemical substances, and energy. The primary emphasis of our investigation is centred on three fundamental variables: temperature, carbonation duration, and system pressure. Upon implementing the methodological framework of response surface methodology (RSM), a comprehensive investigation into the intricate dynamics, adsorption modelling, and cyclic stability assessment of the synthesized adsorbents is conducted. The novelty of this study is that it employs a multifaceted approach to evaluate and optimize a novel adsorbent for carbon capture applications. It employs the usage of coal fly ash to synthesize value added sorbents. It begins with a comparison of various synthesis methods, followed by a first-level screening using BET data to assess adsorption characteristics. The adsorbent is then refined through a second-level screening, optimizing its composition by varying the Na-A and ZIF-8 ratio. Standardization of the response surface methodology (RSM) process is achieved through the CCD spherical experimental design. Subsequently, the RSM process is optimized to enhance carbon capture efficiency. The study explores the effect of TEPA loading on carbon capture uptake and analyzes the influence of temperature on TEPA loading. Cyclic stability tests assess the long-term performance over 50 cycles, while process kinetics modeling, breakthrough curve analysis, and adsorption isotherm modeling provide insights into the dynamic behavior and equilibrium relationships. Amine quantity determination through thermogravimetric analysis (TGA) and amine surface density calculations further contribute to a comprehensive understanding of the adsorbent's synthesis, performance, and key parameters.

2. Materials and methods

All the materials and synthesis methods are mentioned in detail in the ESI.†

2.1. Characterization tools

Several analytical techniques were employed for in-depth material analysis. Fourier transform infrared (FTIR) analysis was conducted using the Jasco FTIR-4200, which offered a range spanning from 400 to 4000 nm with a remarkable resolution of ± 0.5. High precision was ensured with a wavenumber accuracy of ± 0.01 cm^{-1}. The FTIR setup was equipped with a Ge/KBr beam splitter and a DLATGS detector along with DRA-81 accessory. Surface area analysis, using the Brunauer–Emmett–Teller (BET) method, was carried out with the Microtrac Bel SORP mini II instrument. This process was guided by the BEL SORP mini software. X-ray diffraction (XRD) analysis was conducted using the Rigaku ULTIMA-IV model, covering an angle range of 5–100° and employing a Cu X-ray source. Data collection was facilitated by both a scintillation counter and a dTex detector. Field emission scanning electron microscopy (FE-SEM) was performed with the FEI Apreo LoVac instrument. A versatile detector configuration, including the

retractable STEM 3+ detector and DBS detector, was used. Furthermore, our FE-SEM was equipped with an energy dispersive X-ray spectroscopy (EDS) system, specifically the Aztec Standard EDS system, for comprehensive elemental analysis.

2.2. Experimental set-up

The experimental setup for this study was carefully designed to investigate the adsorption process. It consisted of several essential components and instruments to ensure precise and controlled conditions.

The central component of the arrangement featured an adsorption column with a fixed bed, serving a critical function in the adsorption process. To maintain controlled and consistent temperatures throughout the experiment, an electric furnace was integrated into the system. Gas supply lines were thoughtfully connected to the setup, ensuring a steady and dependable source of gases for the adsorption procedure. For the fine-tuning of gas flow rates, mass flow controllers were effectively employed, guaranteeing precise gas flow regulation. The system's temperature conditions were diligently assessed and continually monitored using a thermocouple system, ensuring compliance with the desired range. The inlet of a quartz reactor tube was interconnected with the gas lines, functioning as the fixed bed adsorber. Quartz was deliberately chosen as the tube material due to its exceptional resistance to chemical reactions. Within the quartz tube, quartz wool served as a supportive medium for the adsorbent, effectively preventing the entrainment of adsorbent particles in the gas flow during the reaction. For additional security against the loss of adsorbent particles, a cyclone separator was affixed to the reactor tube's exit, proficiently separating solid particles from the exiting gas. Following cooling, the gas underwent analysis *via* a gas analyzer, enabling a comprehensive examination of its composition. This step was pivotal in assessing the efficiency of the adsorption process and determining the percentage of CO_2 in the exit gas. To provide a visual overview of the setup, a schematic representation of the entire experimental system is presented in Fig. 1. The overall gas flow rate was consistently maintained at 150 mL min^{-1}, while the CO_2 flow rate was kept at 25 mL min^{-1}. To optimize the gas analyzer's performance, a fixed 5 : 1 ratio between nitrogen (N_2) and CO_2 was established. The operating pressure was fixed at 1 bar, with the use of a back pressure regulator to facilitate adsorption experiments at elevated pressures.

3. Physico-chemical attributes

3.1. N_2 adsorption isotherm analysis

The N_2 adsorption isotherm experiments were conducted at 77 K and yielded information regarding the porosity and surface area characteristics of the various adsorbents under investigation. Notably from Table 1, ZIF-8 emerged as the frontrunner in this study, displaying the most remarkable BET surface area at 1580 $m^2 g^{-1}$, a clear indication of its exceptional capacity for gas adsorption at low temperatures. Moreover, ZIF-8 also boasted the largest pore volume among the materials, measuring a substantial 0.79 $cm^3 g^{-1}$, which further underscored its suitability for gas adsorption applications.

In contrast, ZIF-8 synthesized *via* the simultaneous method exhibited a significantly lower BET surface area, registering at only 78 $m^2 g^{-1}$. This discrepancy highlighted the impact of synthesis methods on the resultant materials, with the simultaneous synthesis method yielding a material with comparatively lower porosity. However, it is crucial to consider the presence of Na-A in both ZIF-8@Na-A *via* simultaneous synthesis and ZIF-8@Na-A *via in situ* synthesis. The descending order of surface area is clear: ZIF-8 leads with the highest surface area, followed by ZIF-8@Na-A *via in situ* synthesis, ZIF-8@Na-A *via* physical binding, and finally, ZIF-8@Na-A *via* simultaneous synthesis with the lowest surface area. It is noteworthy that the surface area of ZIF-8@Na-A was found to be lower than that of its parent material, ZIF-8, which can be attributed to the formation of ZIF-8 nanocrystals over the surface of Na-A, effectively reducing the accessible surface area. Overall, these findings provide valuable

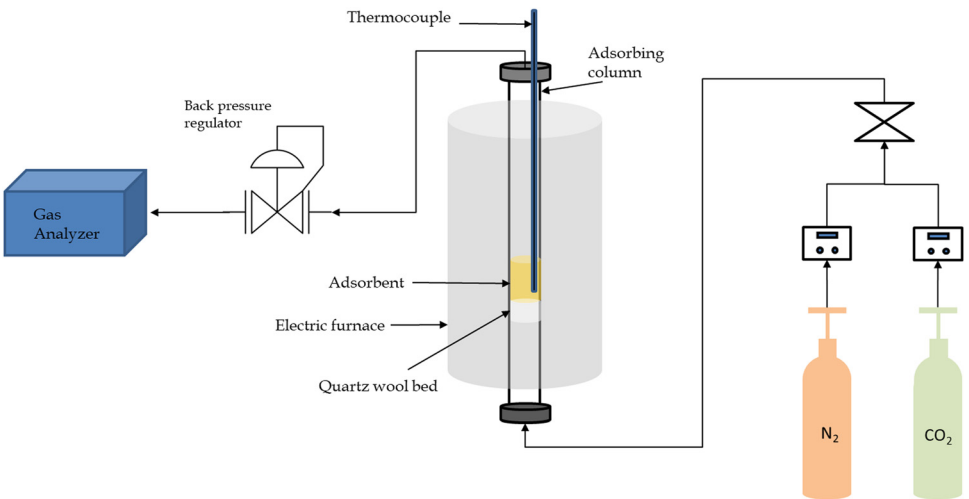

Fig. 1 Experimental set-up.

Table 1 BET surface area of selected adsorbents

Adsorbent	BET surface area (m^2 g^{-1})	Mesopore volume (cc g^{-1})	Micropore volume (cc g^{-1})
ZIF-8	1584	0.09	0.67
Na-A	231	0.04	0.10
ZIF-8@Na-A SM	72	0.001	0.04
ZIF-8@Na-A IM	476	0.04	0.28
ZIF-8@Na-A *via* PM	188	0.03	0.08

insights into the materials' properties and their potential applications in gas adsorption and separation processes, highlighting the intricate relationship between synthesis methods and the resultant materials' characteristics.

The BET surface area of the composite synthesized by physical blending was found to be less than that of either parent material because the components were simply mixed without achieving uniform distribution at the nano level. The BET method calculates specific surface area relative to the mass of the adsorbent, and the lack of evenness in the physical blend resulted in a lower overall surface area. For the composite synthesized *via* the simultaneous synthesis method, the chemical synthesis process itself was uneven and haphazard, preventing the formation of the ordered structures characteristic of the parent materials, leading to a decreased surface area. This is also evidenced by the SEM images (Fig. 2), which show the irregular and disordered morphology of the composite, further corroborating the reduced surface area findings.

3.2. Electron micrographs

Scanning electron micrographs show the topological and the morphological characteristics of ZIF-8, Na-A, ZIF-8@Na-A (*in situ* method) and ZIF-8@Na-A under simultaneous method, presented in Fig. 2. Pure ZIF-8 showed ordered particle structures. The structure of ZIFs is determined mostly by the ratio between the ligand and the metal. The Na-A synthesized exhibited well-defined cuboid-like structures with a relatively smooth morphology. Moreover, the internally produced Na-A displayed consistent particle sizes ranging from 100 nm to 150 nm.[27] The morphology of the synthesized Na-A predominantly relied on the chemical ratio employed during synthesis. In contrast, the synthesized ZIF-8 exhibited dodecahedral structures. The successful synthesis of ZIFs also hinged on the crucial mole ratio between the metal ion and the organic linker. Notably, a Zn : Hmim ratio of 1 : 8 resulted in more disordered and interconnected ZIF-8 particles, while a Zn : Hmim ratio of 1 : 70 yielded well-ordered nanocrystals. Interestingly, the simultaneous synthesis of ZIF-8@Na-A led to a distinct morphology that did not resemble either parent material's ordered structure. This departure from expected morphology might be attributed to the uneven crystal formation inherent in the simultaneous synthesis process. The resulting ZIF-8@Na-A composite showcased the characteristic cuboid particles associated with Na-A, yet it also contained meticulously ordered ZIF-8 nanocrystals forming over the surface of the Na-A particles, as depicted in the accompanying figure. Surprisingly, the geometry of these nanocrystals within the composite was more distinct compared to pure ZIF-8 nanocrystals.

The transmission electron micrographs (Fig. 3) also agreed with the scanning electron micrographs. The micrographs showed that the pure Na-A structures were largely not hollow, *i.e.*, did not consist of structures with high BET surface area and

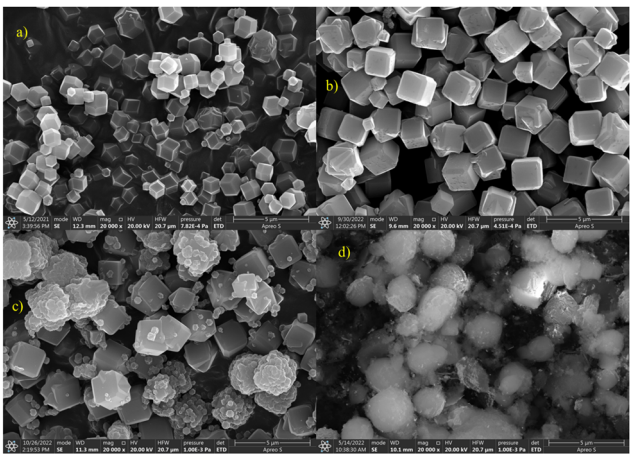

Fig. 2 Micrographs of (a) ZIF-8, (b) Na-A, (c) ZIF-8@Na-A IM and (d) ZIF-8@Na-A SM.

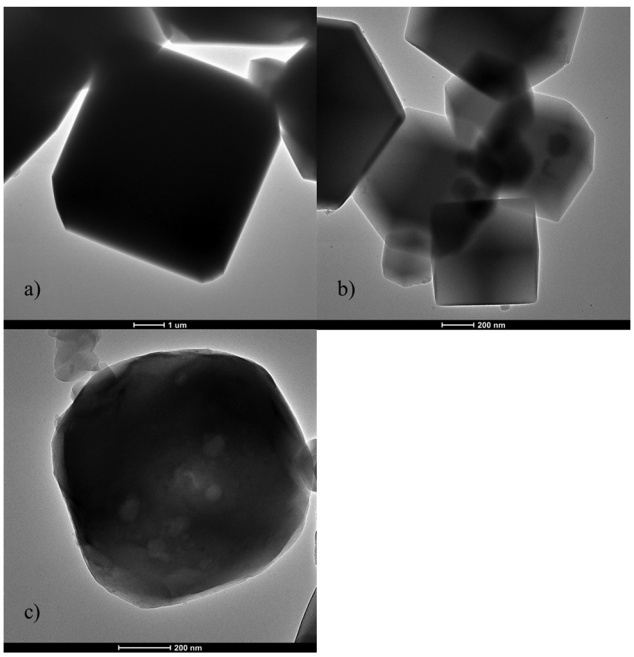

Fig. 3 Transmission electron micrographs of (a) Na-A, (b) ZIF-8, and (c) ZIF-8@Na-A IM 1 : 5.

porosity. This is also consistent with the BET surface area value obtained for the Na-A in Table 1. However, the morphologies obtained by both SEM and TEM are perfectly aligned for Na-A. This structural type is also similar to the Na-A, synthesized from halloysite minerals synthesized by Zhao and team[28] for the purpose of NH_4^+ ion separation within feed water. Yuija *et al.*[29] also synthesized similar Na-A structures using hydrothermal synthesis with pure chemicals and PEG. As for ZIF-8, it can be clearly observed that the in-house synthesized ZIF-8 was transparent indicating a high degree of porosity and high specific surface area, once again in agreement with the N_2 adsorption isotherms presented in Fig. 3 and Table 1. These crystals were extremely similar to the ones obtained by Liyong Chen and group[30] in their study of photocatalytic properties of Au@ZIF-8. Also, Luanwuthi *et al.*[31] synthesized similar hollow and porous ZIF-8 structures for the separation of ferrocene methanol.

The ZIF-8@Na-A 1 : 5 sorbent showed two distinct types of crystal structures. The opaque Na-A structures were clearly visible in the imaging. But on top of the Na-A, hollow and light ZIF-8 grains were also visible. This is a clear indication that ZIF-8 structures were formed over the surface of the bigger Na-A structures. The HAADF analysis also supported this observation. Fig. 4 shows the HAADF imaging of the various expected elements within the composite adsorbent. Elements expected within the Na-A structure, such as Na, Si, Al and O, were found to be clustered around clump areas of the composite image. This is a strong indication that these areas have Na-A structures within them. But surrounding these clusters are layers of Zn, C and N, elements found in the ZIF-8 structure. In fact, these elements even acted as a link between two Na-A clusters, hence proving that ZIF-8 formed over the surface of the existing Na-A crystals.

3.3. XRD diffractograms

The diffractograms presented in Fig. 5 provide valuable insights into the crystalline structures of the materials under investigation. In particular, the diffractograms reveal distinctive peaks that are characteristic of each material, shedding light on their unique structural properties.

In the case of ZIF-8, a series of well-defined peaks were observed at specific angles. Notably, these peaks were detected at 7.291°, 10.325°, 12.702°, 14.673°, 16.431°, 18.003°, 23.281°, and 28.654°. These peaks correspond to specific planes within

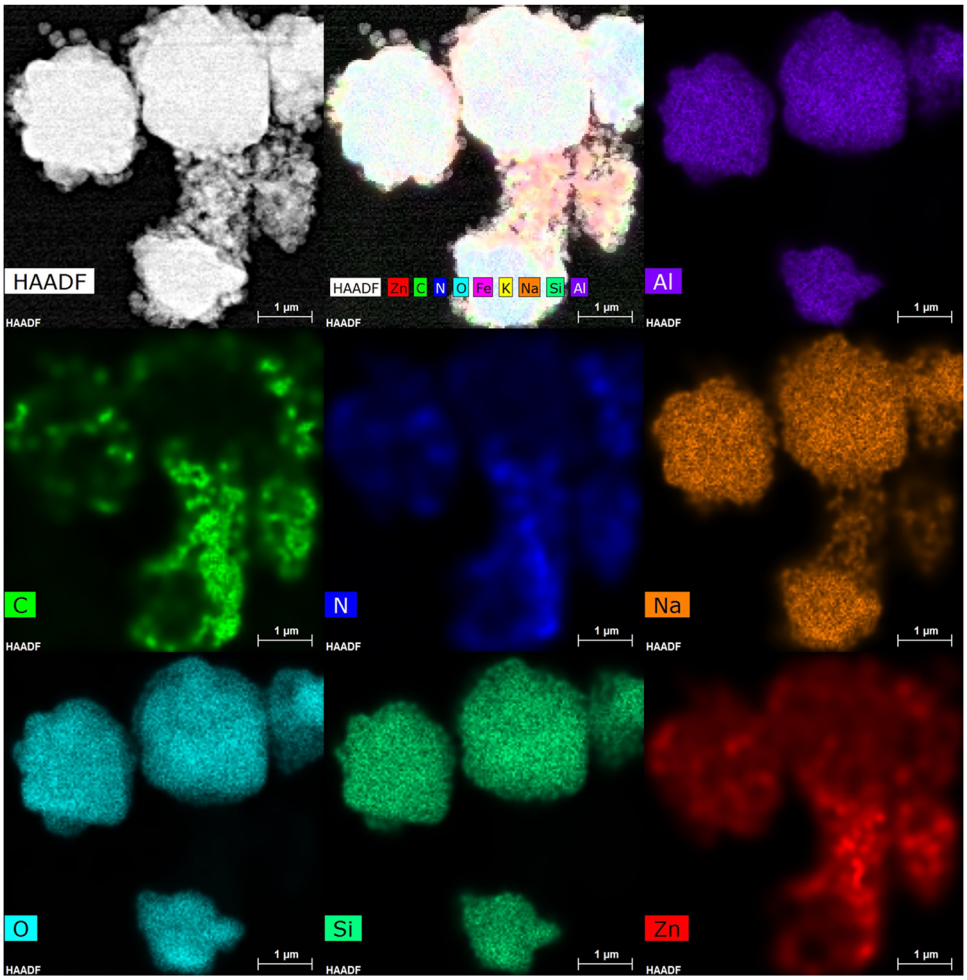

Fig. 4 HAADF imaging of ZIF-8@Na-A IM 1 : 5.

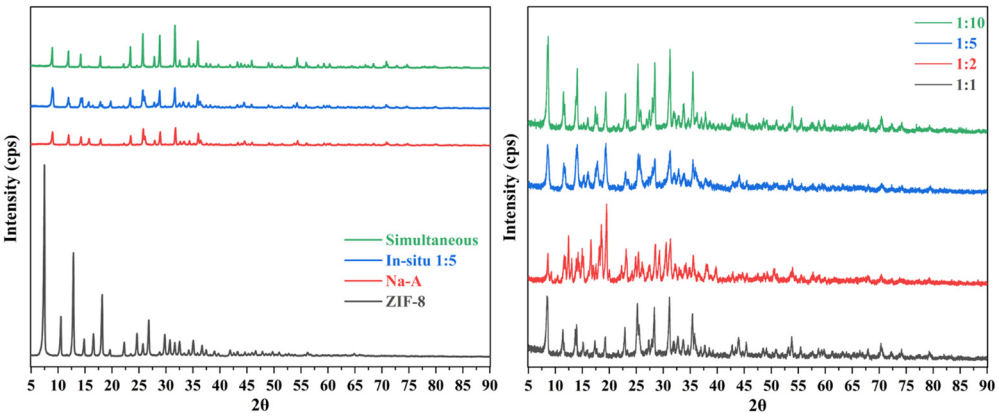

Fig. 5 Diffractograms of synthesized adsorbents.

the crystal lattice structure of ZIF-8. For instance, the peak at 7.291° is indicative of the (011) plane, while the peak at 10.325° corresponds to the (002) plane. Similarly, the peak at 12.702° is associated with the (112) plane, and the peak at 16.431° is attributed to the (013) plane. Furthermore, the peak at 18.003° signifies the presence of the (222) plane.[32]

However, when considering the ZIF-8@Na-A adsorbent, it was evident that these characteristic peaks shifted slightly. The diffractogram revealed peaks at angles 9.031°, 11.917°, 12.097°, 14.210°, 14.468°, 15.694°, 16.442°, 17.842°, 18.178°, 19.751°, 22.113°, 23.407°, 23.860°, 25.720°, 25.971°, 27.34°, 27.823°, 28.381°, 28.825°, 31.6674°, 32.544°, 33.201°, 34.232°, 35.08°, and 35.878°. These shifted peaks indicate changes in the crystallographic structure compared to pure ZIF-8. The presence of Na-A in the composite is believed to influence these shifts, possibly through interactions with the ZIF-8 structure.

In the case of the coal fly ash-based Na-A material, its diffractogram displayed prominent peaks at angles 8.968°, 11.949°, 14.253°, 15.736°, 17.888°, 21.520°, 22.200°, 23.480°, 24.620°, 25.789°, 26.083°, 27.904°, 28.920°, 31.746°, 32.641°, 33.336°, 34.350°, 35.110°, and 35.975°. These peaks align with established literature on the synthesis of Na-A from fly ash[33] and Novembre *et al.*,[34] reaffirming the material's crystallographic characteristics.

The dominance of characteristic Na-A peaks in the diffractogram of the ZIF-8@Na-A sorbent is an intriguing observation. This phenomenon can be attributed to the significant presence of Na-A within the composite material. Essentially, the abundance of Na-A appears to have played a pivotal role in shaping the diffractogram of the composite, effectively overshadowing the typical signature peaks of ZIF-8 during its synthesis process. This finding underscores the intricate interplay between the individual components in the composite. It suggests that the presence of Na-A exerts a profound influence on the structural characteristics and crystalline properties of the composite material. The unique interactions between ZIF-8 and Na-A within the composite are evidently reflected in the diffractogram, providing compelling evidence of these structural transformations. In essence, the dominance of Na-A peaks in the diffractogram serves as a clear indication of the composite's complex and interdependent crystalline properties.

4. Hierarchical optimization of the material and process

4.1. Adsorbent optimization

4.1.1. Adsorbent optimization based on the synthesis protocol. Level I screening of adsorbents was done on the basis of their synthesis methods and properties. Various synthesis methods produce different kinds of morphologies for the same type of adsorbent. Often these properties could be the deciding factor in determining the CC uptake values. Here, three synthesis methods were compared in terms of CC uptake along with the BET surface area. The results are tabulated in Table 2. The initial experimental conditions for the carbon capture uptake studies were as follows: temperature = 298 K, pressure = 1 bar, CO_2% in the feed = 16.7% and gas feed flow rate = 150 mL min^{-1}.

From Table 2, it is evident that pure ZIF-8 displayed high surface area and pore volume. Even when compared to the next best surface area shown by ZIF-8@Na-A synthesized *via* the *in situ* method, the difference is apparent. The ZIF-8@Na-A adsorbents synthesized *via* simultaneous and physical binding methods recorded values much lesser than that of the ZIF-8@Na-A *via* the *in situ* method. However, when the initial CC

Table 2 Results of first level screening

Adsorbent	CC uptake (mmol g^{-1})	BET surface area (m^2 g^{-1})	Mesopore volume (cc g^{-1})	Micropore volume (cc g^{-1})
ZIF-8	1.12	1584	0.09	0.67
Na-A	1.82	230	0.04	0.10
ZIF-8@Na-A SM	1.63	72	0.001	0.04
ZIF-8@Na-A IM	3.48	476	0.04	0.28
ZIF-8@Na-A PB	2.38	236	0.08	0.10

uptake values are brought into the picture, the differences are obvious. Pristine ZIF-8, despite having the highest surface area, recorded the lowest CC uptake value (1.12 mmol g^{-1}) out of the four tested adsorbents. Furthermore, the ZIF-8@Na-A *via* the *in situ* method recorded the highest CC uptake of 3.48 mmol g^{-1}. The key point to note here is that ZIF-8 in this method has been forced to crystallize on the surface of the resident Na-A. This could have contributed to an optimal combination of the physical properties of ZIF-8 and the high chemical affinity of Na-A towards CO_2 in general. ZIF-8@Na-A synthesized *via* simultaneous synthesis recorded the lowest of the surface area and the second lowest CC uptake. This could be due to the incomplete crystallization of both Na-A and ZIF-8 during the synthesis. ZIF-8@Na-A IM demonstrated a lower specific surface area but a significantly higher CO_2 uptake compared to pristine ZIF-8, indicating a superior performance despite the reduced surface area. When compared to the other synthesized composites, namely ZIF-8@Na-A SM and ZIF-8@Na-A PB, ZIF-8@Na-A IM not only showed the highest CC uptake but also possessed a greater specific surface area. This suggests that ZIF-8@Na-A IM is the most effective composite in terms of both CO_2 adsorption capacity and surface area. Consequently, the overall trend is ZIF-8@Na-A IM > ZIF-8@Na-A PB > ZIF-8@Na-A SM in both CO_2 uptake and BET surface area. This highlights the superior structural and adsorption properties of ZIF-8@Na-A IM among the tested materials.

4.1.2. Adsorbent optimization based on Zn^{2+}. Level II screening of adsorbents was done on the basis of the ratio between $Zn(NO_3)_2{\cdot}6H_2O$ and Na-A during the time of synthesis. For example, an adsorbent was designated as ZIF-8@Na-A *via in situ* method 1 : 10, if the ratio of Zn^{2+} to Na-A was 1 : 10 during synthesis. Here, five such ratios were considered and were compared in terms of CC uptake. The results are tabulated in Table 3. The initial experimental conditions for the carbon capture uptake studies were as follows: temperature = 298 K, pressure = 1 bar, CO_2% in the feed = 16.7% and gas feed flow rate = 150 mL min^{-1}.

From the results tabulated in Table 3 and from Fig. 6, the adsorbent with the ratio of 1 : 10 displayed the highest CC uptake. It would also be interesting to note that the 1 : 5 adsorbent was a close second, indicating that after a certain initial synthesis ratio, the increase in CC uptake was nominal. Here, the increase in the quantity of Zn^{2+} proved to be the deciding factor. The lower the Zn^{2+} content, the higher the CC uptake. The content of Na-A was constant in all these adsorbents, indicating that along with the highly basic nature of Na-A, the quantity of pores and the available surface area were also a key factor in determining the CC uptake. So, in line with this reasoning, the 1 : 1 adsorbent recorded the lowest CC uptake out of the four tested adsorbents. Higher quantities of Zn^{2+} may have deprived the CO_2 molecules of additional sites to invade and thus get trapped. Fan Yang and group[35] also synthesized a group of hybrids consisting of zeolite LiX and ZIF-8. In that study too, the amount of ZIF-8 controlled the CO_2 uptake values. The highest uptake value amongst those hybrids was recorded by the LiX@ZIF-8 I sorbent (3.2 mmol g^{-1}) whilst the least uptake was shown by the LiX@ZIF-8 III sorbent (1.6 mmol g^{-1}). From here on, the adsorbent, in focus of this study, would be ZIF-8@Na-A IM 1 : 5 for all further adsorption studies.

Table 3 Results of second level screening

Adsorbent	CC uptake (mmol g^{-1})	BET surface area (m^2 g^{-1})	Micropore volume (cc g^{-1})	Mesopore volume (cc g^{-1})
ZIF-8@Na-A IM 1 : 10	3.61	711	0.31	0.19
ZIF-8@Na-A IM 1 : 5	3.48	476	0.28	0.04
ZIF-8@Na-A IM 1 : 2	2.57	242	0.09	0.03
ZIF-8@Na-A IM 1 : 1	2.31	188	0.07	0.03

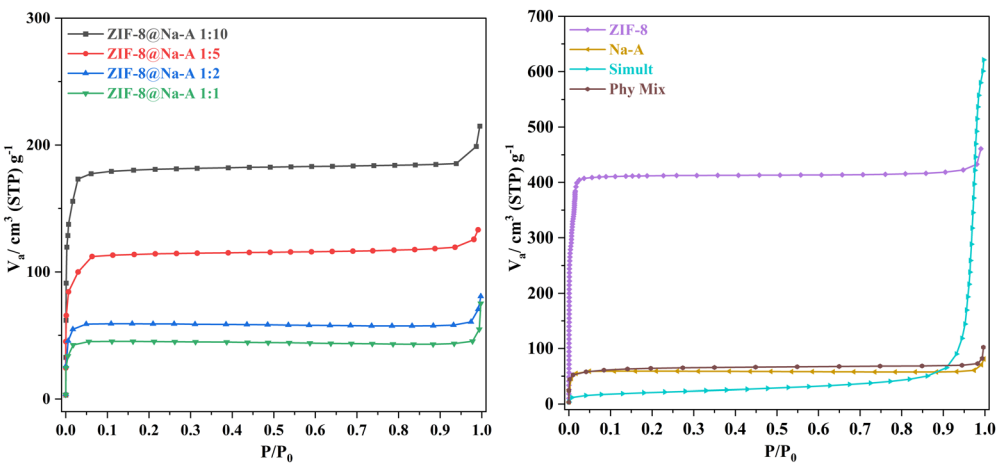

Fig. 6 N_2 adsorption isotherms of synthesized sorbents at 77 K.

4.2. CO_2 uptake standardization

4.2.1. CC uptake experimental design. In this study, RSM was employed to ensure a systematic and well-structured experimental design. The study's primary focus was the investigation of three critical parameters: temperature, pressure, and aeration duration. The rationale behind this experimental design was to gain a comprehensive understanding of how these variables interplayed in the context of carbon capture processes. CCD is a specific type of experimental design used within the framework of RSM. It allows researchers to explore the response surface by varying factors at different levels while considering the potential curvature in the relationship between variables. CCD is particularly effective in identifying optimal conditions for a process by strategically placing experimental runs at the centre and on the surface of a multidimensional response surface. Spherical experimental modelling extends the capabilities of RSM and CCD by incorporating a spherical design, which is characterized by a set of equidistant points on the surface of a hypersphere. This design is particularly useful when studying complex systems with interactions that are not easily captured by linear or quadratic models. The spherical design allows for a more comprehensive exploration of the experimental space, capturing intricate relationships between variables that may be missed in traditional designs.

Within the ambit of temperature variation, a spectrum of temperatures was explored, encompassing the points of 25 °C, 40 °C, 62 °C, 80 °C, and 100 °C. Notably, as the temperature was manipulated and escalated, an interesting and significant trend emerged: there was a discernible decrease in the predicted CC uptake values when the ZIF-8@Na-A adsorbent was employed. This temperature-dependent phenomenon sheds light on the sensitivity of the adsorption process to thermal conditions. One of the noteworthy findings of this study pertains to the comparative performance of ZIF-8@Na-A against pure ZIF-8.[36,37] It is worth emphasizing that one of the inherent challenges in employing MOFs in CC tests is the tendency for the CC values obtained at lower temperatures to exhibit poor cyclic retention. However, the results of this investigation highlighted the superiority of the ZIF-8@Na-A composite adsorbent in addressing this issue. In our previous research endeavor conducted under nearly identical conditions, pure ZIF-8 yielded a CC uptake value of 1.41 mmol g^{-1}. In stark contrast, the composite adsorbent developed in the present study demonstrated a remarkable twofold enhancement in CC performance, thus manifesting its efficacy as an improved adsorbent in the context of carbon capture.

Furthermore, it is noteworthy that these findings are not isolated but resonate with analogous observations from other related studies. For instance, the study conducted by Zhang and co[38] in 2014, which examined CO_2 adsorption employing biochar at elevated temperatures, observed a similar temperature-sensitive behavior. In this investigation, both untreated and CO_2-treated carbonaceous sorbents displayed sorption values of 0.89 mmol g^{-1} and 1.21 mmol g^{-1} at 20 °C, suggesting that temperature significantly influences the adsorption process. Similarly, another study,[39] which delved into the use of zeolites for CO_2 capture, observed similar trends. Both 13-X and WE-G 592 zeolites exhibited consistent CC uptake under varying conditions of CO_2 concentration and total pressure. For instance, at 30 °C and 100 psi, the CC uptake values were approximately 5.0 mol kg^{-1} and 4.5 mol kg^{-1}, respectively. Importantly, when subjected to the same process pressure but at an elevated temperature of 120 °C, these adsorbents retained a substantial portion of their CC uptake values, approximately 72% and 61%, respectively. This retention phenomenon was attributed to a high process pressure and the relatively high partial pressure of CO_2 within the feed gas itself, highlighting the intricate interplay of multiple factors in CC processes.

The role of temperature in influencing adsorption capacity was found to be of paramount importance, rendering it a critical factor to consider. Upon examination of the data presented in Table S1 (ESI†), it became evident that the in-house synthesized adsorbent exhibited superior adsorption capabilities at lower temperatures. This observation aligned with the well-known exothermic nature inherent to physical adsorption processes. When delving further into this phenomenon, it became apparent that as the temperature increased, the interaction between solid and gas molecules at the interface intensified. This heightened interaction could be elucidated by the Boltzmann equation, which attributed it to the increased kinetic energy of the solid–gas molecules engaged in the adsorption process. Consequently, this heightened molecular interaction led to a reduction in the effective and accessible surface area available for adsorption. As a result, it could be reasonably concluded that lower sorption temperatures often yield higher sorption capacities. For adsorbents, optimal temperature for maximizing the adsorption capacity of each adsorbent was mostly the lowest temperature among the available options.

Process pressures were also of five parametric levels: 1.0 bar, 1.6 bar, 2.5 bar, 3.6 bar and 4 bar, as dictated by the RSM CCD spherical model. Indeed, the highest CC uptake of 7.1 mmol g^{-1} was observed at 3.4 bar and 40 °C. Furthermore, at 4 bar process pressure and 62.5 °C, the CC uptake was around 5.8 mmol g^{-1} indicating that process temperature also played an important role in determining the overall CC uptake. Wang *et al.*[40] reported that for their own rice husk synthesized Na-A, the process pressure contributed to a higher CC value. K Yang *et al.*[41] also observed that when the process pressures increased, the CC uptake values of their Y1302 adsorbent increased by 300%. Cheung and group[42] also recorded that for the nano-NaKA adsorbent, an increase in pressure saw the enhancement of the CC uptake value by 100%. Returning to the adsorbents in the present study, as indicated by their N_2 sorption patterns, they are all microporous in nature following the Type-I adsorption pattern (Fig. 6).[43] This would mean that at high process pressures, the pressure difference between the process pressure and the pressure within the narrow micropores of the sorbents would promote high volume CO_2 adsorption quickly. Fig. 7 presents the response surface of the effect of temperature and pressure on CO_2 uptake.

In our investigation, the influence of various operational parameters on CC uptake values was meticulously examined. It

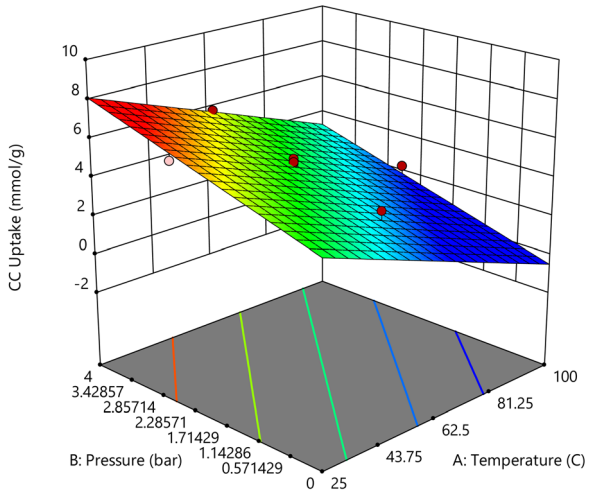

Fig. 7 Response surface of the effect of temperature and pressure on CO_2 uptake.

was apparent that temperature and pressure played pivotal roles in shaping the outcomes of our study. An intriguing observation was made concerning carbonation time which appeared to exert a comparatively modest impact on CC uptake values. In particular, when the extension of carbonation time was undertaken, a slight increment in CC uptake was discerned. However, it is noteworthy that this increment did not amount to much. This is of a similar trend noted by Penchah and team in their research, which centered on the adsorption of CO_2 onto a benzene-based hyper-cross-linked polymer.[44] Further buttressing this trend, a study by Sreenivasulu *et al.* in 2018[45] reported a parallel trend. They found that longer feed times were linked with augmented CC uptake values for the adsorbents they investigated, thereby confirming the affirmative correlation between prolonged contact time and an amplified efficiency in carbon capture.

In summation, while temperature and pressure were identified as fundamental drivers in influencing CC uptake values in our study, the effect of carbonation time and the quantity of adsorbent used, although not negligible, displayed a more subtle influence. These findings resonate with the body of related research within the field, underscoring the pivotal role of contact time in the adsorption process and shedding light on the intricate interplay of diverse parameters in the realm of carbon capture.

A comparison of the performance of the adsorbents reported in the literature with that of the adsorbent developed in the present study is presented in Table 4 in terms of uptake capacity under varying conditions. ZIF-11@ZIF-8 exhibits the highest uptake capacity of 8.21 mmol g^{-1} at 25 °C and 4 bar, making it the most effective under these specific conditions.[46] Conversely, 12.41% ZIF-8@LFNW shows the lowest uptake of 0.20 mmol g^{-1} at 25 °C and 1 bar, indicating limited efficiency. ZIF-8@3wt% g-C3N4 also stands out with a substantial uptake of 7.16 mmol g^{-1}, but this is achieved under more extreme conditions of 45 °C and 15 bar. Other notable adsorbents include CS-ZX aerogel beads with an uptake of 4.23 mmol g^{-1} at 25 °C and 1 bar, and 13X-5CB, which has an uptake of 6.06 mmol g^{-1} at 25 °C and 2 bar. However, the adsorbents that showed higher CC uptake than the one studied in the present work either operated at high process pressures or low process temperatures. These comparisons highlight the significant variations in adsorption capacities and underline the importance of operational conditions in evaluating adsorbent performance.

Table 4 Comparison of various composite adsorbents reported in the literature

S. No.	Adsorbent	Uptake (mmol g^{-1})	Conditions	Ref.
1	LiX@ZIF-8	1.81	25 °C, 1 bar	47
2	ZIF-8@3wt% g-C_3N_4	7.16	45 °C, 15 bar	48
3	ZIF-11@ZIF-8	8.21	25 °C, 4 bar	49
4	CS/ZIF-8/MSNs-525	1.32	25 °C, 1 bar	50
5	12.41% ZIF-8@LFNW	0.20	25 °C, 1 bar	51
6	NaG1.2Z	2.25	35 °C, 1 bar	52
7	CS-ZX aerogel beads	4.23	25 °C, 1 bar	53
8	13X-5CB	6.06	25 °C, 2 bar	54
9	G-NaX	4.32	25 °C, 14 bar	55
10	PC_2-Z	4.50	0 °C, 1 bar	56
11	K_2CO_3/FA aerogel	2.02	20 °C, 1 bar	57
12	CFAZ@ZIF-8	2.83	25 °C, 1 bar	58
13	ZIF-8@MCM-41	3.03	25 °C, 1 bar	59
14	(Ce, Zn) ZIF-8	3.71	25 °C, 1 bar	60
15	ZIF-8@Na-A 1 : 5	3.48	25 °C, 1 bar	This work

Whilst examining the influence of temperature and pressure on CO_2 uptake capacity individually, a clear pattern emerged: as the process temperature increases, the CO_2 uptake capacity tends to decrease, while an increase in process pressure results in a corresponding increase in CO_2 uptake. However, when these two factors are considered in tandem, the relationship becomes more nuanced. Studies indicate that the optimal conditions for maximizing CO_2 uptake occur at a combination of high pressure and low process temperatures. For instance, at a pressure of 3.4 bar and a temperature of 40 °C (as reported in Table S1, Std 7, ESI†), the highest recorded CO_2 uptake was 7.10 mmol g^{-1}. This suggests that under these conditions, the material's affinity for CO_2 is significantly enhanced, likely due to the lower temperature facilitating stronger physical adsorption forces and the higher pressure driving more CO_2 molecules into the available adsorption sites. Interestingly, a similar set of conditions—3.4 bar pressure and 40 °C temperature—produced the second highest CO_2 uptake of 6.63 mmol g^{-1} (Table S1, Std 3, ESI†). The only variable between these two experiments was the duration of feed flow. The small difference in uptake between these two conditions implies that while feed flow duration has some effect, its impact is relatively minor compared to the influence of temperature and pressure. Moreover, the data from Std 12 (Table S1, ESI†) provide additional insights. Despite operating at a higher process pressure, the CO_2 uptake was observed to be lower, at 5.8 mmol g^{-1}. This result suggests that the interaction between temperature and pressure is critical, and both must be optimized together to achieve maximum CO_2 uptake. A higher pressure alone is insufficient if the temperature is not appropriately matched to enhance adsorption.

4.2.3. RSM model generation and verification. Table 5 presents the optimal experimental conditions based on RSM studies. The equations presented in this study have successfully demonstrated a clear correlation between the experimental results and several process factors. This correlation has provided valuable insights into the relationship between CC uptake values and these specific parameters. The coded CC equation for ZIF-8@Na-A is presented below. The coded variable A is the temperature, B is the pressure and C is the time. This model represents the variables most likely to affect the adsorption process profoundly. This equation is specific to this adsorbent, selected parameters, the model assumed and the parametric ranges. The verification of these optimal conditions was done by Design Expert software.

$$\text{CC uptake} = 4.2935 - (1.4169 \times A) + (0.856275 \times B) - (0.0236645 \times C)$$

The model F-value for ZIF-8@Na-A was recorded at 24.88, signifying the model's statistical significance. The high level of concordance observed between the predicted R^2 value, which amounted to 0.953, and the adjusted R^2 value, measuring at 0.945, provided strong evidence for a well-fitting model. A comparative analysis between these predicted values and the actual experimental results revealed reasonably favorable fit statistics. Notably, the standard deviation within the context of this experimental model for ZIF-8@Na-A was approximately 0.33. As depicted in Table 5, a noteworthy alignment was observed between the optimized and predicted values and their corresponding experimental counterparts. This alignment lent substantial credence to the efficacy of the RSM experimental design, underscoring its ability to accurately forecast adsorbent uptake levels within the predefined parameter ranges. The results, thus, affirm the successful application of the RSM approach in this study for precise predictions of adsorbent uptake levels within the specified parameter boundaries.

Table 5 Optimal process conditions

Adsorbent	Temp. (°C)	Pressure (bar)	Time (min)	Predicted CC (mmol g^{-1})	Experimental CC (mmol g^{-1})
ZIF-8@Na-A	55	3	120	5.12	4.88

4.3. Enhancement of CC through amine loading

To enhance the CC uptake further, amine loading was done. Amines are well known to be great absorbents for acidic gases like CO_2 and SO_2. In particular, amines like TETA and TEPA are employed frequently to get rid of acidic gases and moisture from flue gas feed supply. To confirm the presence of amine loaded within the adsorbents, FTIR studies were conducted on all four adsorbents. The IR data corresponding to transmittance of all four adsorbents are presented in Fig. 8.

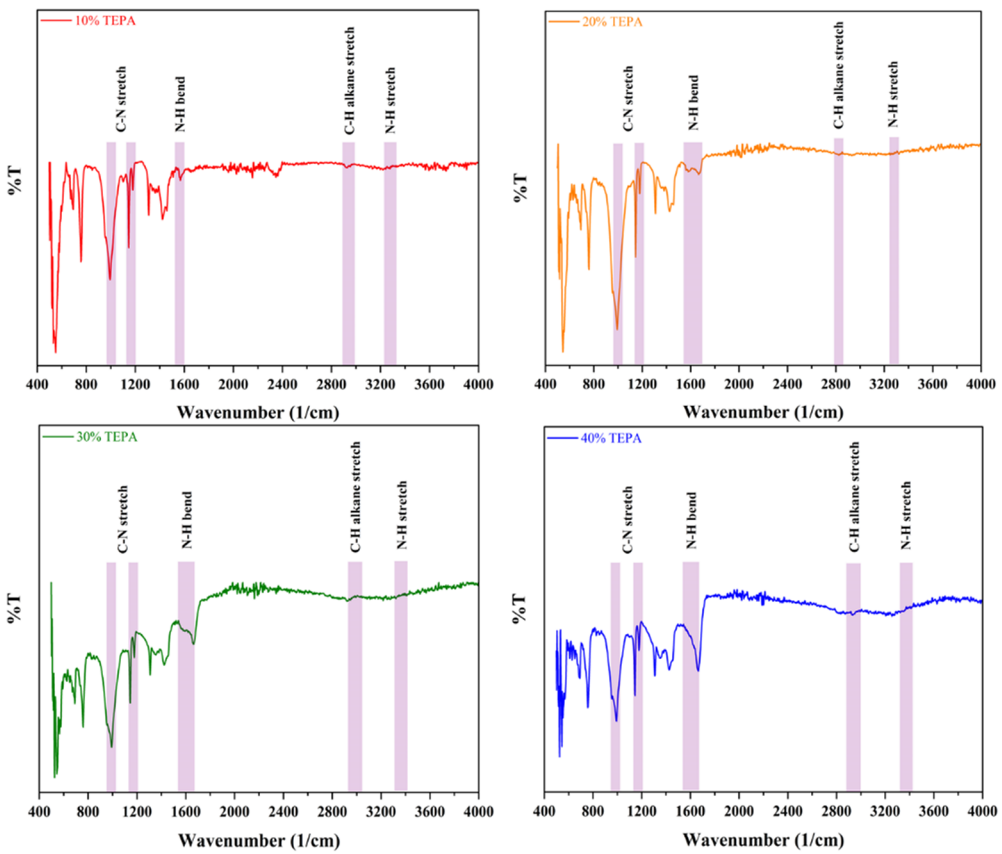

Fig. 8 FTIR peak analysis of TEPA loaded adsorbents.

As expected, all four TEPA loaded adsorbents displayed the strong presence of the secondary amine C–N stretch around 1200 cm^{-1}.[61] The 10%, 20%, 30% and 40% TEPA loaded adsorbents showed this stretch around 1179.07 cm^{-1}, 1178.03 cm^{-1}, 1178.02 cm^{-1} and 1178.03 cm^{-1} respectively (Fig. 8). The corresponding alkane stretch C–H for all these adsorbents was found at 2941.01 cm^{-1}, 2932.86 cm^{-1}, 2920.47 cm^{-1} and 2933.55 cm^{-1}. Traditionally this stretch can be found around 2890 cm^{-1} to 3000 cm^{-1} and this aligns well with the peaks traditionally.[62] The strong N–H bond representing the primary amine stretch is usually found between 1590 cm^{-1} and 1670 cm^{-1} and the secondary N–H stretch around 3200 cm^{-1} to 3450 cm^{-1}.[63] For the adsorbents studied here, the primary N–H bend peaks were observed at 1597.31 cm^{-1}, 1665.70 cm^{-1}, 1664.41 cm^{-1} and 1665.26 cm^{-1} and the secondary N–H stretch peaks were observed at 3267.00 cm^{-1}, 3221.39 cm^{-1}, 3219.08 cm^{-1} and 3265.35 cm^{-1} respectively.

To properly evaluate the extent of amine loading and the decomposition stability of the TEPA loaded adsorbents, thermo-gravimetric analysis was performed. This analysis was done from room temperature to 600 °C with a 10° min^{-1} heating rate, and the data are given in Fig. 9. The samples were taken at various time intervals during the experimental CO_2 analysis to determine the weight loss with the increase in temperature. The first step of decrease for these TEPA loaded adsorbents was recorded between 100 °C and 170 °C.[64] This is mostly associated with the removal of water vapour and other volatile components. This loss was around 5 to 11% depending on the loading percentage. The 10% loaded adsorbent showed only around 5% at this step indicating the lower volume of H_2O adsorbed. On the other hand, both 30% and 40% loaded adsorbents showed a high weight loss due to a higher volume of H_2O adsorbed per unit mass. The second step of significant weight loss was observed between 200 °C and 400 °C. This is attributed to the amine loss from the adsorbent. The boiling point of TEPA is around 330 °C as per IUPAC, but the amine degradation would begin at much lower temperatures due to the instability of amines. This instability resulted in a huge weight loss with respect to the amount of adsorbent considered. For instance, the weight loss determined for the 40% TEPA loaded adsorbent demonstrated a decrease of 35%, which more or less aligned with the initial loading percentage. A similar alignment could be observed with both 20% and 30% TEPA loaded adsorbents as well. Only the 10% loaded adsorbent demonstrated a loss of around 13% within the temperature range mentioned. This could be due to the fact that ZIF-8 itself shows significant degradation at this temperature. In a study done by Harpreet Kaur *et al.*,[65] ZIF-8 nanoparticles showed significant material degradation at temperatures greater than 200 °C. This coupled with amine degradation could have affected the weight loss. Another interesting observation was that, for both 30% and 40% TEPA loaded adsorbents, both Step-I and Step-II seemed to converge into a single step, while for the 10% and 20% TEPA loaded adsorbents both steps were distinct. This could be due to the fact that both 30% and 40% TEPA loaded adsorbents had larger volumes of CO_2 adsorbed and consequently took longer to release the adsorbed CO_2. Amine loading density was also computed to determine the amine loading throughout the adsorbent surface. The amine quantity was verified using the above TGA data. The surface amine density was computed to be around 0.0111 mmol of N m^{-2} for the 10% TEPA loaded adsorbent, 0.0129 mmol of N m^{-2} for the 20% TEPA loaded adsorbent, 0.0198 mmol of N m^{-2} for the 30% TEPA loaded adsorbent and 0.0317 mmol of N m^{-2} for the 40% TEPA loaded adsorbent.

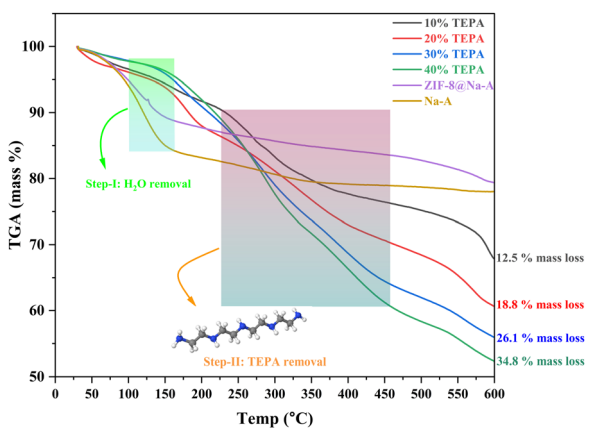

Fig. 9 TGA analysis of the TEPA loaded adsorbents.

4.3.1. Effect of TEPA loading on CC uptake (constant temperature). The study revealed that TEPA loading had a positive impact on the overall CC uptake values, showing a distinct trend of enhanced uptake with increasing TEPA loading. Notably, the CC values exhibited a substantial escalation, particularly when transitioning from 0% TEPA loading to 40% TEPA loading. For instance, the CC value of 3.75 mmol g^{-1} at 10% loading surged to 5.01 mmol g^{-1} at 40% TEPA loading. This observation is consistent with a well-established trend that an augmentation in amine loading typically leads to an increase in CC uptake.

This trend finds support in the research conducted by Taheri and team involving TEPA-loaded mesoporous nanosilica tubes.[66] They reported a remarkable upsurge in CC, particularly when the TEPA loading was increased from 10% to 30%. Specifically, a TEPA loading of 30% resulted in a calculated CC of approximately 9 mmol g^{-1}. Similarly, Li and group observed a similar correlation when they investigated TEPA loading from 25% to 60%, which resulted in a 20% increase in CC values. In that study, the highest CC uptake, reaching 4.02 mmol g^{-1}, was attained for Na-A loaded with 60% TEPA.[67] An intriguing case emerged from the CC uptake study of TEPA loaded onto mesoporous silica gels, conducted by Zhao and his research team.[68] They noted that as TEPA loading increased from 0% to 20%, CC uptake values experienced a notable increase of 27%. However, when the TEPA loading was further elevated from 20% to 50%, the CC uptake displayed a contrasting trend, decreasing by 28%. This decline was attributed to the consequences of excessive amine loading. While an increase in TEPA loading initially enhances CC uptake due to a higher content of basic amines, an excessive rise in

amine loading can lead to pore blockage, reducing the available pore volume and active adsorption sites. Furthermore, an excessive amine loading can result in an uneven dispersion of amines across the surface and pores of the parent adsorbent.

Amines themselves are chemisorbents and thus actively absorb CO_2 through a chemical reaction. ZIF-8 and Na-A, on the other hand, are both solid adsorbents, and their CO_2 uptake is governed by physisorption, which relies on physical interactions rather than chemical bonds. Consequently, when amines are impregnated onto solid supports or physisorbents, the resulting sorption process is almost always a combination of both physisorption and chemisorption. In this context, TEPA plays a crucial role. TEPA is a strong chemisorbent, meaning it reacts chemically with CO_2 to form stable compounds, thereby contributing significantly to the chemisorption aspect of the composite's sorption process. The incorporation of TEPA into a solid support like ZIF-8 or Na-A enhances the overall CO_2 capture efficiency by leveraging the strengths of both sorption mechanisms. The solid support, being a physisorbent, provides a high surface area and porous structure that facilitates the initial capture of CO_2 molecules through weaker, reversible physical interactions. Simultaneously, the impregnated amines (such as TEPA) chemically react with the CO_2 molecules, forming stable carbamate or bicarbonate compounds. This chemisorption process is more robust and ensures a higher capacity for CO_2 capture, as it involves the formation of chemical bonds, which are typically stronger and more stable than the physical interactions governing physisorption. Thus, the combination of physisorption and chemisorption in such a composite material allows for an efficient and effective CO_2 capture system. The physisorbent component (ZIF-8 or Na-A) captures CO_2 molecules through physical interactions, while the chemisorbent (TEPA) ensures a higher overall capture capacity through chemical reactions. This synergistic approach maximizes the advantages of both mechanisms, leading to improved performance in CO_2 capture applications.

4.3.2. Effect of temperature and TEPA loading on CC uptake (constant TEPA loading). The effect of temperature on CC uptake of the 40% TEPA loaded ZIF-8@Na-A 1 : 5 adsorbent is shown in Fig. 10. The TEPA loaded version of ZIF-8@Na-A gave the highest CC uptake value at 60 °C. For example, the 40% TEPA loaded ZIF-8@Na-A showed an uptake value of 5.01 mmol g^{-1} at 25 °C. It then increased considerably to 5.89 mmol g^{-1} at 60 °C and decreased greatly to 4.71 mmol g^{-1} at 100 °C. Liu *et al.*[69] conducted a thorough investigation of the CC uptake activity of the TEPA loaded Al-Fumarate MOF. In their study, the CC uptake for the 50% TEPA loaded Al-Fum MOF increased from 2.00 mmol g^{-1} at 45 °C to 3.40 mmol g^{-1} at 60 °C. But from 60 °C to 100 °C, the CC uptake decreased from 3.40 mmol g^{-1} to 1.50 mmol g^{-1}. This is also in line with our own study. Similarly, Zhang *et al.*[70] also conducted extensive studies on the CC behaviour of amine loaded porous silica. The TEPA loaded porous silica showed a considerable increase for the 60% TEPA loaded adsorbent from 3.75 mmol g^{-1} at 30 °C to 5.01 mmol g^{-1} at 75 °C. However, from there the CC uptake sharply decreased to 3.85 mmol g^{-1} at 105 °C. Modified carbon nanotubes impregnated with TEPA also displayed the same behaviour.[71] A 75% TEPA loaded porous silica displayed an increase in CC from 25 °C to 60 °C and a decrease from there to 80 °C. In contrast to physisorption wherein an increase in process temperature is detrimental to CC uptake, in amine loaded sorption processes the trend is usually hard to predict. Since some degree of chemisorption is involved in amine loaded sorbents, a small increase in temperature could result in a better uptake. This is because at optimal temperatures, 60 °C in the present study, amine spreading across the surface of the parent sorbent would be even, thus promoting high CC uptakes. Furthermore, an increase from this optimal temperature would result in a higher kinetic energy in CO_2 molecules, thus decreasing the adsorption uptake values.

5. Thermo-kinetics modelling and analysis

5.1. Adsorption kinetics modelling

To gain deeper insights into the adsorption process under consideration, it is imperative to delve into the realm of kinetic regimes, as they play a crucial role in elucidating the intricacies of adsorption behavior. The study of kinetics is instrumental in distinguishing between physical and chemical adsorption or even a blend of both. Within the framework of this

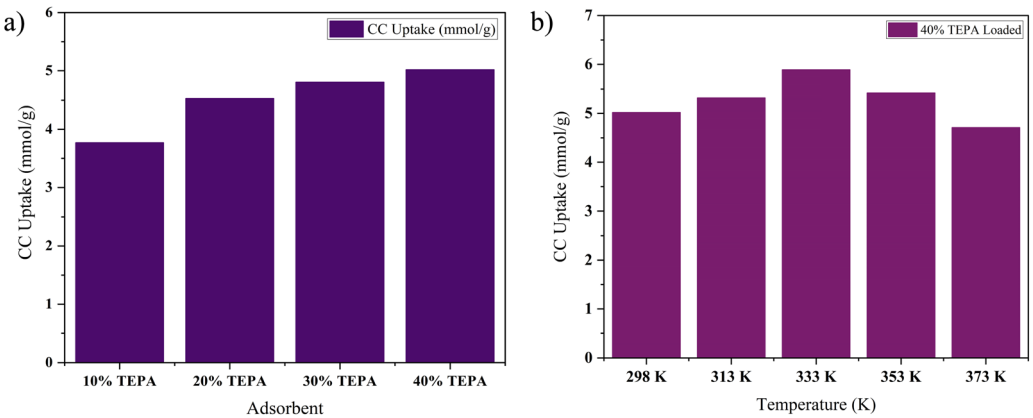

Fig. 10 Effect of (a) TEPA loading and (b) temperature on CC uptake of ZIF-8@Na-A 1 : 5.

investigation, kinetics modeling was carried out for the optimal conditions established in Section 4.2.2. Five kinetic models were applied, encompassing the pseudo first and second orders (PSO), Avrami kinetics, Elovich model, and the Weber–Morris model, which are mathematically expressed by eqn (1)–(5) respectively. These models bear considerable qualitative significance, as they offer valuable insights into the nature of adsorption processes. The PFO model, for instance, typically suggests a predominance of physisorption, which is generally a reversible process. Conversely, a strong concordance with the PSO model within the experimental data often signifies the prevalence of an irreversible chemisorption process governing the adsorption phenomenon. In essence, the employment of these kinetic models provides a comprehensive understanding of the adsorption mechanism at play, shedding light on the balance between physical and chemical interactions, and helping to discern the fundamental nature of the adsorption process.

$$Q_t = Q_e(1 - e^{-k_1 t}) \quad (1)$$

$$Q_t = \frac{Q_e^2 k_2 t}{1 + Q_e k_2 t} \quad (2)$$

$$Q_t = Q_e\left(1 - e^{(-k_a t^n)}\right) \quad (3)$$

$$Q_t = \frac{1}{\beta}\ln[1 + \alpha\beta t] \quad (4)$$

$$Q_t = k_d\sqrt{t} + C \quad (5)$$

The parameters involved in the kinetic models are as follows:

- Q_t: this represents the CC uptake in mmol g^{-1} at a given time 't'.

- Q_e: this signifies the equilibrium CC uptake in mmol g^{-1}, denoting the maximum uptake achievable under the given conditions.

- k_1, k_2, and k_a: these are the rate constants associated with the pseudo first order, pseudo second order, and Avrami kinetics, respectively. They play a crucial role in determining the rate of adsorption or reaction occurring during the process.

- α and β: in the context of the Elovich model, 'α' represents the rate of initial adsorption, while 'β' corresponds to the rate of desorption. These parameters offer insights into the initial adsorption process and the subsequent desorption process.

- K_d: this parameter, known as the Weber–Morris intra-particle diffusion coefficient, pertains to the rate at which the adsorbate molecules or species diffuse within the porous structure of the adsorbent material. It characterizes the intra-particle diffusion process, which is a crucial step in the overall adsorption mechanism.

Fig. 11 and Table 6 offer valuable insights into the kinetics of the adsorption process for the adsorbent at hand. It is evident that the maximum CC capacity for the sorbent is rapidly achieved within just 25 minutes, after which the increase in CC uptake levels off. This behavior can be attributed to the limited retention of NaOH within the adsorbents in comparison to their overall volume. Notably, among the various kinetic models assessed, the Avrami model stands out for its superior fit to the experimental data for the process, as demonstrated in the figure. When comparing the determination coefficient (R^2) of the PFO model to that of the pseudo second-order (PSO) model, both of which are presented in the table, it is evident that the PFO model provides a reasonably good fit for describing the adsorption kinetics. Surprisingly, the Avrami model emerges as the most appropriate model, with an impressively high R^2

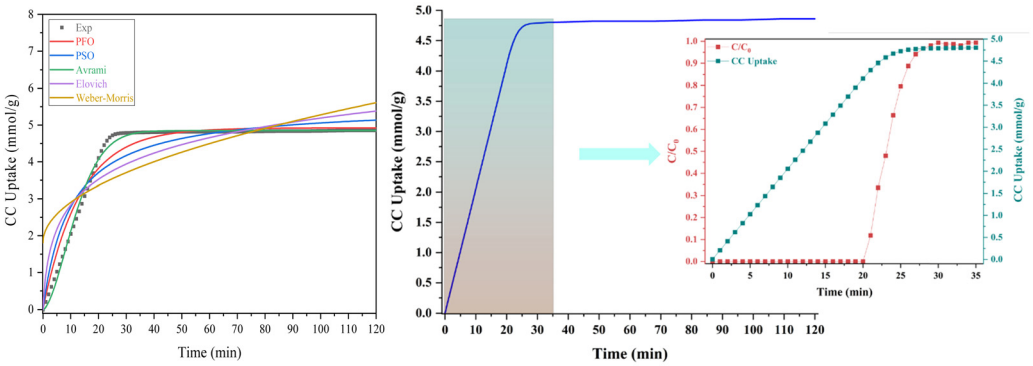

Fig. 11 Kinetics modelling of ZIF-8@Na-A at 328 K, 15% CO_2 and 3 bar total pressure.

Table 6 Kinetic models' parameters at 328 K and 3 bar

Kinetic model	Temp. (K)	Q_e exp. (mmol g^{-1})	Q_e fit (mmol g^{-1})	k	n	C	α	β	R^2
Pseudo first order	328	4.88	4.92	0.0749					0.961
Pseudo second order	328	4.88	5.56	0.0179					0.902
Avrami	328	4.88	4.87	0.0125	1.66				0.994
Elovich	328						1.448	0.951	0.801
Weber–Morris	328			0.3468		1.809			0.605

value of 0.994, indicating the dual nature of the adsorption process, encompassing both physisorption and chemisorption.

Supporting these findings, the study by Yang *et al.*[72] in 2019, focusing on CO_2 adsorption using carbonaceous sorbents pyrolyzed from tree leaves, also found that the PFO model accurately characterizes the adsorption kinetics. Similarly, a research work[73] investigating CO_2 adsorption onto activated carbons observed a close alignment with pseudo first-order kinetics, consistent with the findings of Yang *et al*. Additionally, in a subsequent study conducted by the same research group in 2020,[74] examining CO_2 adsorption onto yellow tuff, the PFO model was once again confirmed as a suitable descriptor. Furthermore, it is important to consider that the predominantly microporous nature of the adsorbent resulted in a swift initial adsorption rate, followed by a sharp deceleration as the micro-pores reached saturation. The Avrami model emerged as the most suitable option for describing the experimental data in comparison to the other models tested.

5.2. Adsorption isotherm modelling

The concentration of CO_2 is a crucial determinant in sorption uptake and plays a pivotal role in defining the point of adsorbent bed saturation. In Fig. 11, partial pressures of CO_2 were adjusted in the range of 0 to 0.8 bar while maintaining a constant temperature of 298 K to investigate the influence of CO_2 concentration on the adsorption process. Our observations revealed that an increase in the CO_2 content in the feed corresponded to a higher quantity of CO_2 being adsorbed. This trend was particularly noticeable as the CO_2 feed percentage increased from 0 to 50, resulting in a nearly threefold increase in CC uptake within this range. However, beyond the 50% mark, the rate of increase became less pronounced, with only a 25% increase in CC uptake levels from 50% to 80%. This phenomenon may be attributed to the fact that, after a certain feed percentage, the adsorption capacity reaches a saturation point, beyond which further increases in CO_2 concentration yield diminishing returns. In line with this observation, Li and group[75] noted a similar trend in their study on the adsorption of CO_2 over activated carbons produced within the temperature range of 540 °C to 800 °C. They found that the enhancement of CC uptake became increasingly marginal as the CO_2 feed percentage increased. This behaviour aligns with materials boasting available surface areas exceeding 500 $m^2\ g^{-1}$, as reported by Wilson and team.[76] Ahmed and group[77] also published findings showing a parallel trend in their investigations with TEPA loaded sorbents. They posited that at low CO_2 partial pressures, the pores of Na-A quickly and readily become filled, while subsequent increases in CO_2 partial pressure result in only marginal additional gains. A similar trend was observed in a study of CO_2 adsorption over pure ZIF-8.[78] Such behavior is typical for materials predominantly characterized by microporous nature, which is consistent with the nature of the ZIF-8@Na-A adsorbent, primarily exhibiting a microporous structure. Guan *et al.*[79] also studied the adsorption isotherm trends of pure ZIF-8 in their published work. In that work, ZIF-8 was found to follow an increasing trend with an increase in CO_2 partial pressure within the feed. The reasons again were attributed to the high microporosity of ZIF-8 itself.

The amount of CO_2 present is a critical factor in sorption uptake and determines when the adsorbent bed saturates. As seen in Fig. 12, partial pressures of CO_2 were adjusted between 0 and 0.8 bar while maintaining a constant temperature of 298 K to examine the impact of CO_2 concentration on the adsorption process. It was found that an increase in the feed's CO_2 content was accompanied by an increase in the amount of CO_2 adsorbed. This tendency was especially noticeable when CO_2 feed percentages rose from 0 to 50, which caused the values of CC uptake within this range to nearly triple. But beyond 50%, the pace of rise became less significant. There was just a 25% rise in CC uptake levels from 50% to 80%. Guan *et al.*[79] also worked on ZIF-8 based adsorbents and even there the uptake values increased with increasing CO_2 concentration. Similarly, McEwen *et al.*[80] also found the same trend. Four isotherm models, *viz.*, the Langmuir model,[81] Freundlich model,[82] Sips model[83] and Toth model,[84] were considered. The Langmuir isotherm model assumes that adsorption occurs at specific sites on the adsorbent surface, and each site can accommodate only one adsorbate molecule. The Freundlich isotherm model is an empirical model that describes multilayer adsorption on heterogeneous surfaces. The Sips isotherm model, also known as the Langmuir-Freundlich or the Langmuir-like model, is a combination of Langmuir and Freundlich models. It allows for both monolayer and multilayer adsorption. The Toth isotherm model is an alternative to the Langmuir model, accommodating multilayer adsorption and heterogeneity.

The mathematical expressions for these isotherms are presented in eqn (6)–(9), respectively.

$$q = \frac{q_e k_L p}{1 + k_L p} \tag{6}$$

$$q = k_F p^{1/n} \tag{7}$$

$$q = \frac{q_m k_s p}{[1 + k_s p^n]} \tag{8}$$

$$q = \frac{q_m k_T p}{[1 + (k_T p)^n]^{\frac{1}{n}}} \tag{9}$$

Within the context of these isotherms,

– 'q' denotes the quantity of CO_2 adsorbed at a specific time 't';

– 'q_m' signifies the monolayer uptake, indicating the maximum capacity of the adsorbent for CO_2 adsorption;

– 'k_L', 'k_F', 'k_S', and 'k_T' represent the adsorption constants associated with the Langmuir, Freundlich, Sips, and Toth isotherms, respectively. These constants play a pivotal role in determining the characteristics of the adsorption process and the affinity of the adsorbent for the adsorbate;

– 'n' is a parameter utilized to measure the heterogeneity in the Sips and Toth models. It provides insights into the

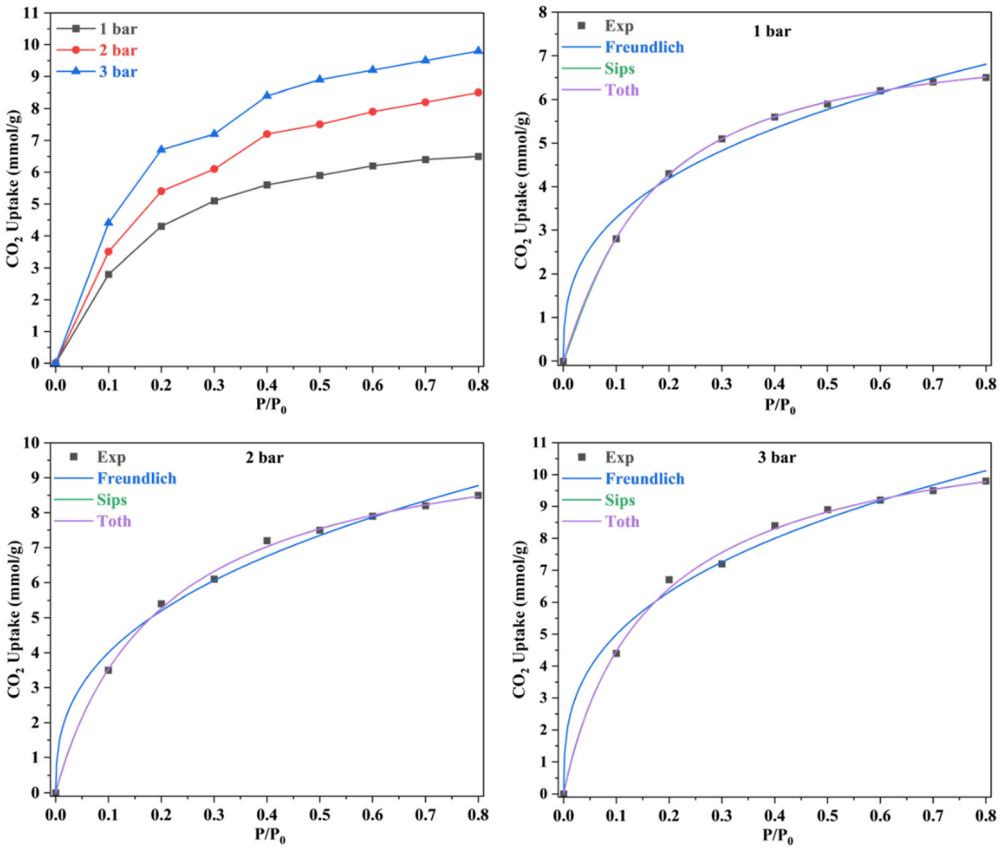

Fig. 12 CO_2 adsorption isotherms of ZIF-8@Na-A at 298 K.

non-uniformity of adsorption sites and the distribution of energies available for adsorption on the adsorbent surface.

The R^2 values presented in Tables 7 and 8 indicate that the Langmuir isotherm model was not a good fit for the adsorbent across all three process pressures. For the ZIF-8@Na-A adsorbent, the Langmuir model did not fit at all for the considered pressures. In contrast, the Freundlich model achieved R^2 values of 0.981, 0.988, and 0.987 at 1 bar, 2 bar, and 3 bar, respectively. Although the Sips model slightly outperformed the Toth model, as shown in Table 8, this suggests a mixed adsorption nature comprising both monolayer and multilayer characteristics. The compatibility of the Sips model with heterogeneous adsorbent surfaces aligns with the composite nature of the adsorbents. The nature of adsorption is heavily influenced by pore characteristics, as illustrated by the study on CO_2 uptake over TEPA-modified TiO_2 by Kapica-Kozar and colleagues.[85] Similarly, in the studies by Azeem *et al.*[86] on KOH activated porous carbons and by Melouki *et al.*[87] on carbons derived from olive waste, the Sips model demonstrated an excellent fit to experimental data, with the Toth model being a close second. Yongha Park *et al.*'s comparative study[88] involving activated carbon and zeolite-LiX for CO_2 uptake also favored the Sips model for both adsorbents. However, Sun *et al.*'s[89] investigation of CO_2 adsorption on graphene with an average pore size of 3 nm highlighted Langmuir adsorption behavior, despite surface multilayer adsorption. Regarding the tested adsorbents, ZIF-8@Na-A 1 : 5 exhibited a microporous nature indicating the presence of narrow, ores

Table 7 Adsorption isotherm modelling fit for the Freundlich model at 298 K

Adsorbent	Total pressure (bar)	Freundlich		
		k_F	n	R^2
ZIF-8@Na-A	1	7.38	2.86	0.981
	2	9.55	2.65	0.988
	3	10.64	2.94	0.987

Table 8 Adsorption isotherm modelling fit for Sips and Toth models at 298 K

Adsorbent	Total pressure (bar)	Sips				Toth			
		k_S	Q_m (mmol g^{-1})	n	R^2	Q_m (mmol g^{-1})	k_T	n	R^2
ZIF-8@Na-A	1	8.4421	7.51	1.15	0.999	4.95	7.5638	1.25	0.998
	2	4.6015	10.75	0.98	0.998	11.77	4.6891	0.95	0.994
	3	5.2541	12.08	0.96	0.998	14.34	5.4513	0.92	0.996

within its structure. Adsorbents with such narrow micropores often exhibit heightened CO_2 uptake rates under high process pressures. ZIF-8, being a framework with these narrow pores, capitalizes on the pressure differential, a pivotal factor for adsorption at elevated pressures. This inherent property makes MOFs and ZIFs well-suited for high-pressure adsorption processes. ZIF-8@Na-A also portrays a primarily microporous character. However, unlike pure ZIF-8, this composite showcases a significant decrease in microporosity. At lower process pressures, the micropores saturate rapidly, following a nearly linear trend. Subsequent increments are marginal, indicating gradual filling of existing mesopores.

5.3. Adsorption thermodynamics

The heat of adsorption was calculated using the Clausius–Clapeyron equation. Three temperatures, specifically 298 K, 313 K, and 328 K, were considered under a process pressure of 1 bar. The resulting plots, illustrating the relationship between $1/T$ (reciprocal temperature) and the natural logarithm of pressure ($\ln P$), are displayed in Fig. 13. These plots allowed valuable insights to be gained into the thermodynamics of the adsorption process and the energetics associated with CO_2 uptake on the surfaces of the adsorbent at various temperatures.

In this investigation, eight distinct uptake values were scrutinized for ZIF-8@Na-A, encompassing a loading range from 1 mmol g^{-1} to 4.5 mmol g^{-1}. The resulting analysis unveiled an average heat of adsorption for the ZIF-8@Na-A adsorbent at these loading levels, yielding a value of approximately −11.05 kJ $kmol^{-1}$. Remarkably, this figure aligns closely with the typical range observed for pure ZIF-8. Fischer and Bell (2014) had previously reported heat of adsorption values for pure ZIF-8 that spanned from −12.0 to −19.5 kJ mol^{-1}, while simulations consistently indicated heat of adsorption values ranging between −14.0 and −19.0 kJ mol^{-1}.[90] A parallel study by Russell and Migone[91] disclosed that the heat of adsorption for modified ZIF-8 structures was around −18 kJ mol^{-1}. Given the favorable fit of the Sips isotherm to our data, it was selected for the calculation of the isosteric heat of adsorption. This parameter serves as a fundamental indicator of the adsorbent's affinity for CO_2 molecules and imparts critical insights into the thermodynamics governing the adsorption process.

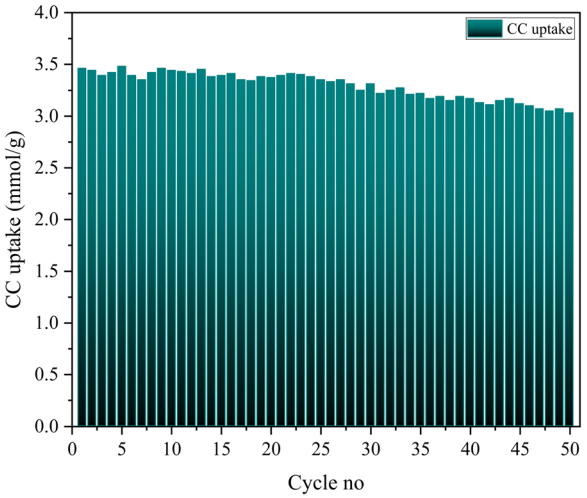

Fig. 14 Cyclic retention capacity of ZIF-8@Na-A at 298 K and 1 bar.

6. Cyclic stability

Cyclic stability tests were carried out to thoroughly assess the durability and performance stability of the adsorbents over repeated usage. In each cycle, a standard sample weighing 5 grams was introduced into the reactor, and carbonation was conducted at a constant temperature of 298 K. The feed gas consisted of a mixture of N_2 and CO_2, with a total feed flow rate of 150 mL min^{-1}, and CO_2 constituted roughly one-sixth of the gaseous feed composition. Following each cycle of carbonation, the process of decarbonation or regeneration was executed at a temperature of 150 °C in an inert atmosphere. The selection of this temperature was deliberate, aimed at preserving the capacity of ZIF-8, as it is known to be sensitive to excessive heat exposure. The cyclic retention performance is graphically presented in Fig. 14. Remarkably, the adsorbent exhibited exceptional stability even after subjecting it to the rigors of 50 cycles of carbonation and regeneration. For the ZIF-8@Na-A adsorbent, which initially demonstrated a CC value of 3.45 mmol g^{-1} at 298 K, its CC uptake after 50 cycles remained impressively high at approximately 3.03 mmol g^{-1}. This level of stability is particularly noteworthy considering the

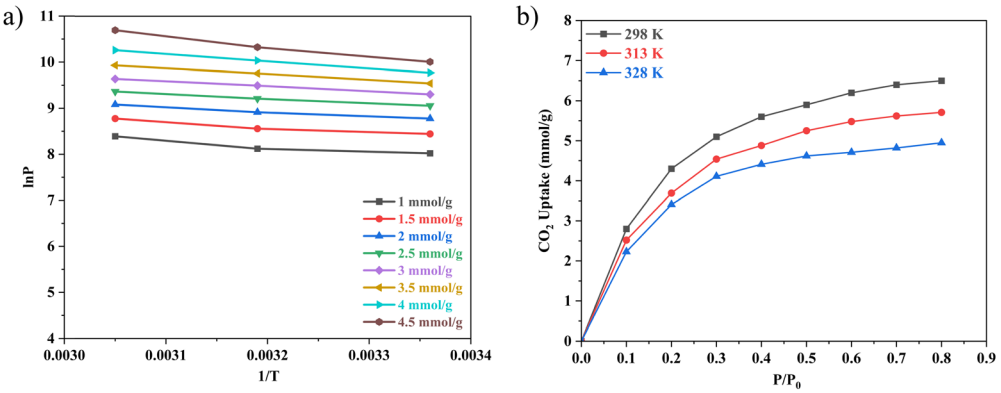

Fig. 13 $1/T$ *vs.* $\ln P$ graph for (a) ZIF-8@Na-A and (b) isotherms at different temperatures.

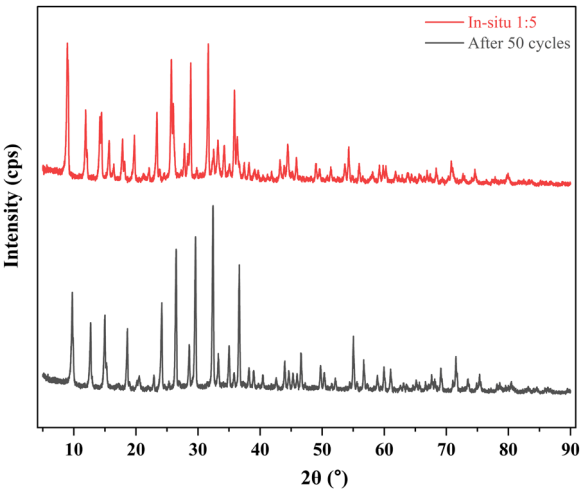

Fig. 15 Diffractograms before and after cyclic stability studies.

inclusion of ZIF-8 within the composite. Generally, zeolitic imidazolate frameworks (ZIFs) and metal–organic frameworks (MOFs) are known to be highly susceptible to degradation when repeatedly exposed to elevated temperatures. Notably, the ZIF-8@Na-A adsorbent exhibited a subtle change in colour, transitioning from its usual white appearance to a very pale tint of yellow after completing 50 cycles. A marginal loss of only nine percentage points over the course of 50 cyclic processes is indeed negligible. The cyclic performance of the adsorbent is visually depicted in Fig. 14, underscoring the remarkable stability achieved even under rigorous testing conditions.

Fig. 15 clearly indicates the diminishing peaks between 7° and 24°, demonstrating the reduction in ZIF-8 intensity. This decrease in peak intensity suggests partial material degradation of ZIF-8 after 50 cycles. The BET surface area values further support this interpretation. Initially, the adsorbent had a specific surface area of 476 m^2 g^{-1}, which decreased to 424 m^2 g^{-1} after 50 cycles. This decline in surface area corroborates the XRD data, indicating that ZIF-8 within the composite underwent partial degradation. The degradation of ZIF-8 can be attributed to the repeated cycling process, which likely causes structural breakdown and loss of crystallinity. This structural degradation is reflected in the XRD patterns, where the characteristic peaks of ZIF-8 become less pronounced. The diminishing intensity of these peaks between 7° and 24° signifies a loss of the ordered crystalline structure, which is essential for maintaining high surface area and porosity. The BET surface area analysis provides quantitative evidence of this structural degradation. The significant drop from 476 m^2 g^{-1} to 424 m^2 g^{-1} after 50 cycles indicates a reduction in the number of available adsorption sites, which is critical for the material's performance in CO_2 capture. This reduction in surface area is directly linked to the loss of the ZIF-8 framework, further supporting the XRD findings. The partial degradation of ZIF-8 has a direct impact on the CO_2 uptake capacity of the adsorbent. As the structural integrity of ZIF-8 diminishes, the material's ability to adsorb CO_2 is compromised. This is because the high surface area and porosity of ZIF-8 are key factors in its efficiency as a CO_2 adsorbent. The combined evidence from XRD and BET surface area analyses clearly indicates that the ZIF-8 within the composite undergoes partial degradation after 50 cycles.

Table 9 shows that the adsorbent synthesized in this study performs better than most other adsorbents. This includes both modified and unmodified adsorbents from the literature. Even after a period of 50 cycles, the adsorbent in the current study performed better than most of the reported sorbents in the table. The LiX@ZIF-8 adsorbent could retain around 71% of its initial CC uptake values after a period of 50 cycles. It is interesting to note from simulation studies that the Mg-MOF-74 adsorbent exhibited a good capture capacity of 5.77 mmol g^{-1} even upto 90 cycles. The rest of the adsorbents showed good retention capacities only for lower durations. Their efficiency for an increased duration time is yet to studied.

7. Conclusions

Through *in situ* synthesis techniques, novel composites were successfully synthesized. Systematic carbon capture (CC) uptake experiments were conducted on these adsorbents, employing RSM for process standardization.

Table 9 Comparison of cyclic stability of reported adsorbents

S. No.	Adsorbent	Initial uptake (mmol g^{-1})	Number of cycles	Cyclic retention (%)	Ref.
1	SZX	1.97	5	99	93
2	Zeolite@carboHIPE	1.35	15	70	94
3	HZ2	4.00	5	99	95
4	HZ4A-1-3	2.75	10	82	96
5	ZIF-8@MCM-41	3.03	15	95	59
6	(Ce, Zn) ZIF-8	3.71	15	94	60
7	HZSM-5/AEEA	4.44	10	75	97
8	NaA-1.0	4.34	10	99	98
9	Mg-MOF-74	5.77	90	95	92
10	IBA-Z4A	2.50	5	99	99
11	PEI/MCS/PEG	4.25	10	95	100
12	50 wt% MgO@ZIF-8	1.30	5	88	101
13	15TETA/ZIF-8	2.45	4	95	102
14	LiX@ZIF-8-I	1.75	50	71	35
15	ZIF-8@Na-A 1 : 5	3.48	50	92	This work

• BET analysis revealed that the ZIF-8@Na-A adsorbent demonstrated a diminished surface area compared to its parent materials. This decrease in surface area was further confirmed by scanning electron micrographs, which clearly depicted the presence of ZIF-8 formed upon the surface of Na-A.

• An increase in TEPA loading had a positive impact on CC uptake, with the maximum uptake achieved at a TEPA loading of 40%.

• Process pressure exhibited a favourable effect on CC uptake, with the highest recorded CC uptake values occurring at 3 bar pressure.

• The adsorption models derived through CCD modeling were found to align exceptionally well with the experimental data. Experiments conducted at the optimal values recommended by the CCD model closely matched the standard deviation values predicted by the model, affirming the reliability of the model's predictions.

• The Avrami model for kinetics provided a highly effective description of the adsorption kinetics, as indicated by an R^2 value of 0.994.

• Sips adsorption modelling proved to be a robust method for explaining the experimental data, suggesting a combination of monolayer and multilayer adsorption mechanisms.

• The average heat of adsorption, calculated at -11.78 kJ mol^{-1}, underscored the predominantly physical nature of the adsorption process, revealing that it was driven primarily by physisorption interactions.

• Impressively, the adsorbent exhibited exceptional cyclic performance, retaining over 92% of its initial adsorption capacities even after 50 cycles. Notably, ZIF-8@Na-A exhibited a subtle change in colour, shifting to a slightly pale-yellow hue after these repeated cycles, which may indicate the possibility of thermal alteration in response to the cyclic conditions.

In the realm of future research, there exists an exciting opportunity to delve deeper into the intricate relationship between synthesis parameters and the physicochemical attributes of composite materials. Specifically, key factors such as the metal-to-ligand ratio, the selection of synthesis temperature, and the choice of solvent are poised to take the centre stage. These parameters are known to exert a significant influence on the overall morphology and structural characteristics of the composites that have been the subject of this study. Understanding how these variables interact and impact the composite materials can provide valuable insights, not only in terms of optimizing synthesis processes but also in tailoring the properties of these materials for specific applications. This avenue of exploration holds great promise for advancing the field of composite materials and unlocking their full potential in various scientific and industrial domains.

Data availability

No primary research results, software or code have been included and no new data were generated or analysed as part of this research work.

Conflicts of interest

The authors declare that they have no known competing financial interests or personal relationships that could have appeared to influence the work reported in this paper.

Acknowledgements

The authors extend their heartfelt gratitude to the Council of Scientific and Industrial Research (CSIR), Government of India, for sponsoring the project under the Scheme 22(0783)/19/EMR-II. They also wish to express their gratitude to BITS Pilani Hyderabad Campus for their invaluable support and facilitation of this project. Furthermore, the authors would like to acknowledge the Central Analytical Laboratory (CAL) at BITS Pilani HYD campus for their indispensable assistance, providing access to the essential analytical tools.

References

1 R. Aniruddha, I. Sreedhar and B. M. Reddy, *J. CO2 Util.*, 2020, **42**, 101297.
2 L. Valencia and H. N. Abdelhamid, *Carbohydr. Polym.*, 2019, **213**, 338–345.
3 J. Wang, S. Cui, Z. Li, S. Wen, P. Ning, S. Lu, P. Lu, L. Huang and Q. Wang, *Chem. Eng. J.*, 2021, **415**, 128859.
4 C. W. Chang, Y. H. Kao, P. H. Shen, P. C. Kang and C. Y. Wang, *J. Hazard. Mater.*, 2020, **400**, 122974.
5 N. E. Tari, A. Tadjarodi, J. Tamnanloo and S. Fatemi, *Microporous Mesoporous Mater.*, 2016, **231**, 154–162.
6 R. Aniruddha and I. Sreedhar, *Environ. Sci. Pollut. Res.*, 2021, **1**, 1–10.
7 B. Sreenivasulu, I. Sreedhar, B. M. Reddy and K. V. Raghavan, *Energy Fuels*, 2017, **31**, 785–794.
8 Z. Zhang, Y. Xiao, B. Wang, Q. Sun and H. Liu, *Energy Procedia*, 2017, **114**, 2537–2544.
9 T. F. de Aquino, S. T. Estevam, V. O. Viola, C. R. M. Marques, F. L. Zancan, L. B. Vasconcelos, H. G. Riella, M. J. R. Pires, R. Morales-Ospino, A. E. B. Torres, M. Bastos-Neto and C. L. Cavalcante, *Fuel*, 2020, **276**, 118143.
10 J. Pokhrel, N. Bhoria, S. Anastasiou, T. Tsoufis, D. Gournis, G. Romanos and G. N. Karanikolos, *Microporous Mesoporous Mater.*, 2018, **267**, 53–67.
11 A. Huang and B. Feng, *Int. J. Hydrogen Energy*, 2018, **43**, 2224–2231.
12 S. Xian, F. Xu, C. Ma, Y. Wu, Q. Xia, H. Wang and Z. Li, *Chem. Eng. J.*, 2015, **280**, 363–369.
13 S. Xian, F. Xu, C. Ma, Y. Wu, Q. Xia, H. Wang and Z. Li, *Chem. Eng. J.*, 2015, **280**, 363–369.
14 E. E. Unveren, B. O. Monkul, S. Sarioglan, N. Karademir and E. Alper, *Petroleum*, 2017, **3**, 37–50.
15 S. Ahsan, A. Ayub, D. Meeroff and M. Jahandar Lashaki, *Chem. Eng. J.*, 2022, **437**, 135139.
16 R. Thiruvenkatachari, S. Su, X. X. Yu and J. S. Bae, *Int. J. Greenhouse Gas Control*, 2013, **13**, 191–200.

17 X. Zhao, Q. Cui, B. Wang, X. Yan, S. Singh, F. Zhang, X. Gao and Y. Li, *Chin. J. Chem. Eng.*, 2018, 2292–2302.
18 N. Hedin, L. Chen and A. Laaksonen, *Nanoscale*, 2010, **2**, 1819–1841.
19 R. Habibi, F. Pourfayaz, M. Mehrpooya and H. Kamali, *Sustainable Energy Technol. Assess.*, 2022, **52**, 101984.
20 M. Marczak-Grzesik, P. Piersa, M. Karczewski, S. Szufa, H. Ünyay, A. Kędzierska-Sar and P. Bochenek, *Energies*, 2021, **14**, 7101.
21 J. Rosen, T. Geary, A. Hilmi, R. Blanco-Gutierrez, C.-Y. Yuh, C. S. Pereira, L. Han, R. A. Johnson, C. A. Willman, H. Ghezel-Ayagh and T. A. Barckholtz, *J. Electrochem. Soc.*, 2020, **167**, 64505.
22 D. Bahamon and L. F. Vega, *Chem. Eng. J.*, 2016, **284**, 438–447.
23 J. Schell, N. Casas, D. Marx, R. Blom and M. Mazzotti, *Energy Procedia*, 2013, **37**, 167–174.
24 X. Zhu, T. Ge, F. Yang and R. Wang, *Renewable Sustainable Energy Rev.*, 2021, **137**, 110651.
25 R. T. Maruyama, K. N. Pai, S. G. Subraveti and A. Rajendran, *Int. J. Greenhouse Gas Control*, 2020, 102902.
26 K. N. Pai, J. D. Baboolal, D. A. Sharp and A. Rajendran, *Sep. Purif. Technol.*, 2019, **211**, 540–550.
27 E. Grabias-Blicharz, R. Panek, M. Franus and W. Franus, *Materials*, 2022, **15**, 7174.
28 Y. Zhao, B. Zhang, X. Zhang, J. Wang, J. Liu and R. Chen, *J. Hazard. Mater.*, 2010, **178**, 658–664.
29 Y. Jiang, H. Qi, J. Wang, X. Sun, C. Lyu, P. Lu, R. Yang, A. Noreen, C. Xing and N. Tsubaki, *Ind. Eng. Chem. Res.*, 2022, **61**, 1725–1732.
30 L. Chen, Y. Peng, H. Wang, Z. Gu and C. Duan, *Chem. Commun.*, 2014, **50**, 8651–8654.
31 S. Luanwuthi, A. Krittayavathananon, P. Srimuk and M. Sawangphruk, *RSC Adv.*, 2015, **5**, 46617–46623.
32 Z. Zhang, S. Xian, H. Xi, H. Wang and Z. Li, *Chem. Eng. Sci.*, 2011, **66**, 4878–4888.
33 Z. Jiang, J. Yang, H. Ma, X. Ma and J. Yuan, *Clean Technol. Environ. Policy*, 2016, **18**, 629–637.
34 D. Novembre, B. di Sabatino, D. Gimeno and C. Pace, *Clay Miner.*, 2011, **46**, 339–354.
35 F. Yang, J. Wu, X. Zhu, T. Ge and R. Wang, *Chem. Eng. J.*, 2021, **410**, 128322.
36 P. F. Liu, K. Tao, G. C. Li, M. K. Wu, S. R. Zhu, F. Y. Yi, W. N. Zhao and L. Han, *Dalton Trans.*, 2016, **45**, 12632–12635.
37 T. Chokbunpiam, S. Fritzsche, C. Chmelik, J. Caro, W. Janke and S. Hannongbua, *J. Phys. Chem. C*, 2016, **120**, 23458–23468.
38 X. Zhang, S. Zhang, H. Yang, Y. Feng, Y. Chen, X. Wang and H. Chen, *Chem. Eng. J.*, 2014, **257**, 20–27.
39 R. V. Siriwardane, M. S. Shen, E. P. Fisher and J. Losch, *Energy Fuels*, 2005, **19**, 1153–1159.
40 Y. Wang, T. Du, H. Jia, Z. Qiu and Y. Song, *Solid State Sci.*, 2018, **86**, 24–33.
41 K. Yang, G. Yang and J. Wu, *Chem. Eng. J.*, 2021, **404**, 127056.
42 O. Cheung, Z. Bacsik, Q. Liu, A. Mace and N. Hedin, *Appl. Energy*, 2013, **112**, 1326–1336.
43 S. Lowell and J. E. Shields, *Powder Surface Area and Porosity*, 1991, pp. 11–13.
44 H. Ramezanipour Penchah, A. Ghaemi and H. Ganadzadeh Gilani, *Energy Fuels*, 2019, **33**, 12578–12586.
45 B. Sreenivasulu, I. Sreedhar, A. S. Singh and A. Venugopal, *Energy Fuels*, 2018, **32**, 3716–3725.
46 S. R. Hosseini, M. Omidkhah, Z. Mehri Lighvan, S. Norouzbahari and A. Ghadimi, *Sep. Purif. Technol.*, 2023, **307**, 122679.
47 F. Yang, X. Zhu, J. Wu, R. Wang and T. Ge, *Powder Technol.*, 2022, **399**, 117090.
48 A. U. Khan, T. Noor, N. Iqbal, N. Zaman and Z. Hussain, *J. Mater. Sci.*, 2023, **58**, 3947–3959.
49 S. R. Hosseini, M. Omidkhah, Z. Mehri Lighvan, S. Norouzbahari and A. Ghadimi, *Sep. Purif. Technol.*, 2023, **307**, 122679.
50 L. Yin, D. Li, S. Li, F. Gai, T. Zhang, Y. Liu and X. Zhao, *J. Dispers. Sci. Technol.*, 2023, **44**, 2303–2310.
51 Y. Shi, G. Tian, R. Ni, L. Zhang, W. Hu and Y. Zhao, *Sep. Purif. Technol.*, 2023, **322**, 124356.
52 M. Boscherini, F. Miccio, E. Papa, V. Medri, E. Landi, F. Doghieri and M. Minelli, *Chem. Eng. J.*, 2021, **408**, 127315.
53 E. Luzzi, P. Aprea, M. S. De Luna, D. Caputo and G. Filippone, *ACS Appl. Mater. Interfaces*, 2021, **13**, 20728–20734.
54 E. Khoramzadeh, M. Mofarahi, K. Chung and C. H. Lee, *Sep. Purif. Technol.*, 2022, **280**, 119917.
55 S. Candamano, A. Policicchio, G. Conte, R. Abarca, C. Algieri, S. Chakraborty, S. Curcio, V. Calabrò, F. Crea and R. G. Agostino, *J. Cleaner Prod.*, 2022, **330**, 129843.
56 F. Gan, B. Wang, Z. Jin, L. Xie, Z. Dai, T. Zhou and X. Jiang, *Sci. Total Environ.*, 2021, **768**, 144529.
57 B. Guo, J. Zhang, Y. Wang, X. Qiao, J. Xiang and Y. Jin, *Energy*, 2023, **263**, 125764.
58 R. Aniruddha and I. Sreedhar, *Environ. Sci. Pollut. Res.*, 2023, **30**, 8393–8402.
59 R. Aniruddha, I. Sreedhar and B. M. Reddy, *J. CO2 Util.*, 2022, **64**, 102182.
60 R. Aniruddha, V. M. Shama, I. Sreedhar and C. M. Patel, *J. Cleaner Prod.*, 2022, **350**, 131478.
61 Y. Cao, F. Song, Y. Zhao and Q. Zhong, *J. Environ. Sci.*, 2013, **25**, 2081–2087.
62 K. M. Gilbert, E. N. Kirby, I. Escala, Z. Yuan, M. Du, M. S. R. M. Nasir, M. P. Khairunnisa, N. W. C. Jusoh and A. A. Jalil, *IOP Conf. Ser.: Mater. Sci. Eng.*, 2020, **808**, 012031.
63 A. Alkhouzaam, H. Abdelrazeq, M. Khraisheh, F. Almomani, B. H. Hameed, M. K. Hassan, M. A. Al-Ghouti and R. Selvaraj, *Nanomaterials*, 2022, **12**, 1240.
64 Q. Ye, J. Jiang, C. Wang, Y. Liu, H. Pan and Y. Shi, *Energy Fuels*, 2012, **26**, 2497–2504.
65 H. Kaur, G. C. Mohanta, V. Gupta, D. Kukkar and S. Tyagi, *J. Drug Delivery Sci. Technol.*, 2017, **41**, 106–112.
66 F. S. Taheri, A. Ghaemi and A. Maleki, *Energy Fuels*, 2019, **33**, 11465–11476.
67 S. Li, S. Jia, T. Nagasaka, H. Bai and L. Yang, *Sustainability*, 2023, **15**, 10144.
68 P. Zhao, G. Zhang, Y. Xu and Y. Lv, *J. CO2 Util.*, 2019, **34**, 543–557.

69 Q. Liu, Y. Ding, Q. Liao, X. Zhu, H. Wang and J. Yang, *Colloids Surf., A*, 2019, **579**, 123645.
70 G. Zhang, P. Zhao and Y. Xu, *J. Ind. Eng. Chem.*, 2017, **54**, 59–68.
71 M. Irani, A. T. Jacobson, K. A. M. Gasem and M. Fan, *Fuel*, 2017, **206**, 10–18.
72 G. Yang, S. Song, J. Li, Z. Tang, J. Ye and J. Yang, *J. Mater. Sci. Technol.*, 2019, **35**, 875–884.
73 P. Ammendola, F. Raganati and R. Chirone, *Chem. Eng. J.*, 2017, **322**, 302–313.
74 P. Ammendola, F. Raganati, R. Chirone and F. Miccio, *Powder Technol.*, 2020, **373**, 446–458.
75 D. Li, J. Zhou, Y. Wang, Y. Tian, L. Wei, Z. Zhang, Y. Qiao and J. Li, *Fuel*, 2019, **238**, 232–239.
76 S. M. W. Wilson, F. Al-Enzi, V. A. Gabriel and F. H. Tezel, *Microporous Mesoporous Mater.*, 2021, **322**, 111089.
77 S. Ahmed, A. Ramli, S. Yusup and M. Farooq, *Chem. Eng. Res. Des.*, 2017, **122**, 33–42.
78 D. Liu, Y. Wu, Q. Xia, Z. Li and H. Xi, *Adsorption*, 2013, **19**, 25–37.
79 Y. Guan, J. Shi, M. Xia, J. Zhang, Z. Pang, A. Marchetti, X. Wang, J. Cai and X. Kong, *Appl. Surf. Sci.*, 2017, **423**, 349–353.
80 J. McEwen, J. D. Hayman and A. Ozgur Yazaydin, *Chem. Phys.*, 2013, **412**, 72–76.
81 S. Alafnan, A. Awotunde, G. Glatz, S. Adjei, I. Alrumaih and A. Gowida, *J. Pet. Sci. Eng.*, 2021, **207**, 109172.
82 Gautam, R. P. Sah and S. Sahoo, *Sādhanā*, 2023, **48**, 1–37.
83 L. Feng, Y. Shen, T. Wu, B. Liu, D. Zhang and Z. Tang, *Adsorption*, 2020, **26**, 1101–1111.
84 C. Chilev, M. Dicko, P. Langlois and F. Lamari, *Metals*, 2022, **12**, 1698.
85 J. Kapica-Kozar, B. Michalkiewicz, R. J. Wrobel, S. Mozia, E. Piróg, E. Kusiak-Nejman, J. Serafin, A. W. Morawski and U. Narkiewicz, *New J. Chem.*, 2017, **41**, 7870–7885.
86 A. Sarwar, M. Ali, A. H. Khoja, A. Nawar, A. Waqas, R. Liaquat, S. R. Naqvi and M. Asjid, *J. CO2 Util.*, 2021, **46**, 101476.
87 R. Melouki, A. Ouadah and P. L. Llewellyn, *J. CO2 Util.*, 2020, **42**, 101292.
88 Y. Park, D. K. Moon, Y. H. Kim, H. Ahn and C. H. Lee, *Adsorption*, 2014, **20**, 631–647.
89 J. Sun, C. Chen, Y. Zhang, W. Li and Y. Song, *Chem. Eng. J.*, 2022, **430**, 133172.
90 M. Fischer and R. G. Bell, *CrystEngComm*, 2014, **16**, 1934–1949.
91 B. Russell and A. Migone, *Microporous Mesoporous Mater.*, 2017, **246**, 178–185.
92 N. A. A. Qasem and R. Ben-Mansour, *Appl. Energy*, 2018, **230**, 1093–1107.
93 T. F. de Aquino, S. T. Estevam, V. O. Viola, C. R. M. Marques, F. L. Zancan, L. B. Vasconcelos, H. G. Riella, M. J. R. Pires, R. Morales-Ospino, A. E. B. Torres, M. Bastos-Neto and C. L. Cavalcante, *Fuel*, 2020, **276**, 118143.
94 M. Mazaj, M. Bjelica, E. Žagar, N. Z. Logar and S. Kovačič, *ChemSusChem*, 2020, **13**, 2089–2097.
95 M. Kim, J. W. Lee, S. Kim and Y. T. Kang, *J. Cleaner Prod.*, 2022, **337**, 130597.
96 D. Panda, E. A. Kumar and S. K. Singh, *J. CO2 Util.*, 2020, **40**, 101223.
97 H. Cheng, H. Song, S. Toan, B. Wang, K. A. M. Gasem, M. Fan and F. Cheng, *Chem. Eng. J.*, 2021, **406**, 126882.
98 X. Zhou, S. Shi, B. Ding, H. Jia, P. Chen, T. Du and Y. Wang, *Environ. Sci. Pollut. Res.*, 2023, **30**, 102803.
99 D. Panda, E. A. Kumar and S. K. Singh, *Ind. Eng. Chem. Res.*, 2019, **58**, 5301–5313.
100 M. Wang, L. Yao, J. Wang, Z. Zhang, W. Qiao, D. Long and L. Ling, *Appl. Energy*, 2016, **168**, 282–290.
101 C. W. Chang, Y. H. Kao, P. H. Shen, P. C. Kang and C. Y. Wang, *J. Hazard. Mater.*, 2020, **400**, 122974.
102 A. Mohammadi and A. Nakhaei Pour, *J. CO2 Util.*, 2023, **69**, 102424.